Toward Improved Understanding of Magnetic Fields Participating in Solar Flares: Statistical Analysis of Magnetic Fields within Flare Ribbons

Maria D. Kazachenko[1,2] , Benjamin J. Lynch[3] , Antonia Savcheva[4,5] , Xudong Sun[6] , and Brian T. Welsch[7]

[1] Dept. of Astrophysical and Planetary Sciences, University of Colorado Boulder, 2000 Colorado Ave., Boulder, CO 80305, USA; maria.kazachenko@colorado.edu
[2] National Solar Observatory, 3665 Discovery Dr., Boulder, CO 80303, USA
[3] Space Sciences Laboratory, University of California, Berkeley, CA 94720, USA
[4] Harvard-Smithsonian Center for Astrophysics, 60 Garden St., Cambridge, MA 02138, USA
[5] Institute of Astronomy and National Astronomical Observatory, Bulgarian Academy of Sciences, 72 Tsarigradsko Chaussee Blvd., 1784 Sofia, Bulgaria
[6] Institute for Astronomy, University of Hawaii at Manoa, 34 Ohia Ku St., Pukalani, HI 96768, USA
[7] Dept. of Natural & Applied Sciences, University of Wisconsin–Green Bay, Green Bay, WI 54311, USA

Abstract

Violent solar flares and coronal mass ejections (CMEs) are magnetic phenomena. However, how magnetic fields reconnecting in the flare differ from nonflaring magnetic fields remains unclear owing to the lack of studies of the flare magnetic properties. Here we present a first statistical study of flaring (highlighted by flare ribbons) vector magnetic fields in the photosphere. Our systematic approach allows us to describe the key physical properties of solar flare magnetism, including distributions of magnetic flux, magnetic shear, vertical current, and net current over flaring versus nonflaring parts of the active region (AR), and compare these with flare/CME properties. Our analysis suggests that while flares are guided by the physical properties that scale with AR size, like the total amount of magnetic flux that participates in the reconnection process and the total current (extensive properties), CMEs are guided by mean properties, like the fraction of the AR magnetic flux that participates (intensive property), with little dependence on the amount of shear at the polarity inversion line (PIL) or the net current. We find that the nonneutralized current is proportional to the amount of shear at the PIL, providing direct evidence that net vertical currents are formed as a result of any mechanism that could generate magnetic shear along the PIL. We also find that eruptive events tend to have smaller PIL fluxes and larger magnetic shears than confined events. Our analysis provides a reference for more realistic solar and stellar flare models. The database is available online and can be used for future quantitative studies of flare magnetism.

Unified Astronomy Thesaurus concepts: Solar active regions (1974); Solar active region magnetic fields (1975); Solar coronal mass ejections (310); Solar flares (1496)

Supporting material: machine-readable table

1. Introduction

Solar flares and coronal mass ejections (CMEs) that produce the most severe space weather disturbances arise from significant reconfiguration of magnetic fields in the solar corona. Because these coronal fields are rooted in the underlying, much denser solar photosphere, understanding how flares and CMEs work requires understanding the structure and evolution of magnetic fields from the photosphere to the corona. Historically, most of the analyses of photospheric magnetic fields before and during the flares focused on the active region (AR) as a whole (e.g., Toriumi & Wang 2019). However, flare observations have shown that only a fraction of the AR magnetic field participates in the flare; from the analysis of 3000 solar flares, we found that the fraction of AR magnetic flux that undergoes reconnection ranges from $(3 \pm 2)\%$ to $(21 \pm 10)\%$ for C1- to X-class flares, respectively (see Figure 12 in Kazachenko et al. 2017). Moreover, subsequent flares can occur in very different areas of the same AR; a well-known example is the two extreme events on 2003 October 28 and 29 that occurred in different locations in AR 10486 (Kazachenko et al. 2010). This implies that to understand why and how flares occur, we need to understand the properties of the magnetic fields that participate in the flare and how they differ from the AR as a whole.

According to the canonical two-dimensional (2D) flare model called the CSHKP model (Carmichael 1964; Sturrock 1968; Hirayama 1974; Kopp & Pneuman 1976) and its extension to 3D (Longcope et al. 2007; Aulanier et al. 2012; Janvier et al. 2014; Savcheva et al. 2015, 2016), maps of flare ribbons identify the footpoints of newly reconnected magnetic fields (see Figure 1). In relation to magnetic topology, ribbons correspond to locations where separatrices, dividing domains of distinct connectivity, like spines and fans (Longcope et al. 2007; Kazachenko et al. 2012), or quasi-separatrix layers (QSLs; Savcheva et al. 2015, 2016) intersect with the chromosphere. Until recently, accuracy of both vector magnetic field and ribbon measurements limited the systematic analysis of magnetic fields within flare ribbon areas.

The launch of the Solar Dynamics Observatory (SDO; Pesnell et al. 2012) with the Helioseismic and Magnetic Imager (HMI; Scherrer et al. 2012; Hoeksema et al. 2014) and Atmospheric Imaging Assembly (AIA; Lemen et al. 2012) instruments marks the first time that both a vector magnetograph and ribbon-imaging capabilities became available on the same observing platform, making coregistration of AIA and HMI full-disk data relatively easy. In this paper, we make use of these two instruments and present a database of vector magnetic field properties swept by flare ribbons in 40 flaring events, C-class and larger. Our intentions are twofold. First, we provide the reference information
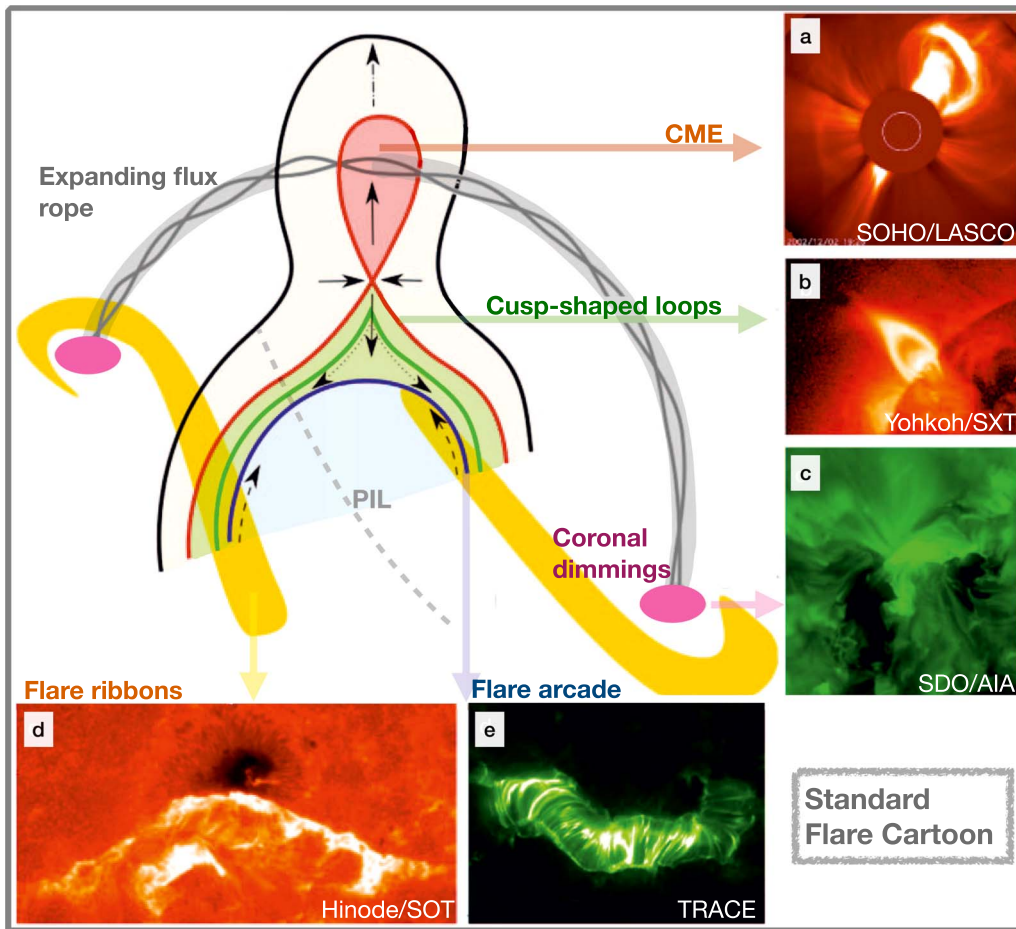
Figure 1. Standard flare cartoon from Savcheva et al. (2016). As the flux rope rises (gray), it stretches the current sheet and the QSLs in the plane perpendicular to the flux rope (red), forming a set of newly reconnected cusped and arcade-shaped field lines (green and blue, respectively) with footpoints, highlighted as flare ribbons (yellow). Images on the right and bottom show the main observed features explained by the model: (a) CME with three-part structure from SOHO/LASCO, (b) cusped loops from Yohkoh/SXT, (c) coronal dimmings from SDO/AIA, (d) flare ribbons from Hinode/SOT, and (e) flare arcade from TRACE. Published with the author's permission.

for the data set by describing the key processing procedures. Second, we present statistical analyses of the photospheric magnetic field participating in the flare and its relationship with that of the polarity inversion line (PIL) and the AR as a whole.

This paper follows the study of Kazachenko et al. (2017), who presented a `RibbonDB` database of 3137 solar flare ribbon events and their area and magnetic fluxes (reconnection fluxes). Complementing our previous study, here we create a new data set, `FlareMagDB`, and describe the vector magnetic field properties: magnetic flux, mean magnetic shear, vertical current, and net current within the flare ribbons and AR and PIL areas.

This paper is organized as follows. In Section 2, we describe the SDO data we use, the list of selected events, and the methods. In Section 3, we describe the statistical results of the `FlareMagDB` analysis. In Section 4, we describe the results of the analysis of the 3D MHD Adaptively Refined MHD Solver (ARMS) simulation. Finally, in Section 6, we discuss the results and summarize the conclusions.

2. Data and Methods

In this section, we describe the data and methods we used to identify various physical properties of the AR magnetic field: identification of the PILs, flare ribbons and AR areas; estimates of the magnetic fluxes, shears, vertical currents and net currents within PIL, ribbons and AR areas.

2.1. Data

We have assembled a `FlareMagDB` catalog that includes 40 flares: 10 X-, 28 M-, and 2 C-class flares (see Table 1). To give an overview of these 40 events, in Figure 2, we show vertical magnetic field maps of 40 ARs hosting these flares. Out of 40 flares, 33 were associated with CMEs (eruptive, 7 X- and 26 M-class flares), and seven were not associated with CMEs (confined, 3 X-, 2 M-, and 2 C-class flares; Yashiro et al. 2006). To select our 40 events, we used the `RibbonDB` flare ribbon catalog that described the reconnection flux properties of 3137 flares (Kazachenko et al. 2017). Our main selection criterion was choosing a sample of events spanning a wide range of ARs and reconnection fluxes of flare class M1.0 and above, representative of the medium and strong flares of the `RibbonDB` catalog. Figure 3 compares `FlareMagDB` events with events from `RibbonDB`; it shows scatter plots of the peak X-ray flux versus unsigned AR, ribbon, and PIL magnetic fluxes for events in both databases.

For each event in the database, we use (1) a preflare HMI/SDO vector magnetogram of $ds_{\mathrm{HMI}} = 0''5$ spatial resolution, $\boldsymbol{B}(x, y) = (B_x, B_y, B_z)(x, y)$, to find magnetic field

Table 1
FlareMagDB Database: Magnetic Field Properties of 40 Flares within the AR, Ribbon, and PIL Areas

i	T_{start}	Flare Class	AR Number	H +/−	Φ, 10^{20} Mx			$\overline{\alpha}$, 10^3 G°			$I_{z,u}$, 10^{12} A			$|DC/RC|$			V_{CME} km s^{-1}
					AR	rbn	PIL	AR	rbn	PIL	AR	rbn	PIL	AR	rbn	PIL	
00	2010-08-07 17:55	M1.0	11093	−1	64	12	0.1	8.4	12.0	11.0	45	4.8	0.0	1.0	1.3	1.9	871
01	2011-02-15 01:44	X2.2	11158	1	139	53	5.5	12.8	25.1	51.5	49	13.8	3.6	1.1	1.5	1.7	669
02	2011-08-03 13:17	M6.0	11261	1	127	23	7.2	11.9	18.5	34.5	61	9.5	5.7	1.2	1.6	4.2	610
03	2011-09-06 22:12	X2.1	11283	1	122	23	1.3	7.8	20.9	41.7	48	7.7	0.8	1.1	2.0	3.2	575
04	2011-10-02 00:37	M3.9	11305	−1	87	10	2.3	7.7	16.3	34.9	37	3.6	1.5	1.2	2.0	2.8	259
05	2011-11-15 12:30	M1.9	11346	−1	67	06	1.1	7.4	15.1	19.2	123	5.5	1.1	1	1.8	1.9	300
06△	2011-12-27 04:11	C8.9	11386	1	74	04	0.7	7.7	10.5	13.1	170	3	0.8	1.1	1.0	1.6	⋯
07	2012-01-19 13:44	M3.2	11402	−1	215	10	2.9	10.7	17.9	21.8	230	5.0	2.6	1.0	1	1.2	1120
08	2012-01-23 03:38	M8.7	11402	−1	222	35	3.5	10.7	16.9	21.2	160	18.2	3.3	1.0	1.1	2.1	2175
09	2012-03-07 00:02	X5.4	11429	−1	188	76	12.4	14.3	29.3	41.3	124	27.2	7.7	1.1	1.6	2.0	2684
10	2012-03-09 03:22	M6.3	11429	−1	212	59	5.6	12.3	19.1	43.1	99	14.7	3.4	1.2	1.8	4.4	950
11	2012-03-10 17:15	M8.4	11429	−1	184	58	3.0	12.9	18.8	32.5	87	19.0	2.4	1.2	1.4	2.3	1379
12	2012-03-14 15:08	M2.8	11432	1	74	12	0.3	7.9	10.8	9.1	30	3.5	0.2	1.0	1.1	0.7	411
13	2012-07-12 15:37	X1.4	11520	1	356	40	7.6	15.5	22.1	29.4	94	6.6	3.9	1.2	1.7	1.9	885
14	2012-11-21 06:45	M1.4	11618	−1	132	15	4.9	11.4	23.5	30.0	37	4.3	3	1.2	2.3	2.4	410
15	2013-04-11 06:55	M6.5	11719	−1	123	19	0.2	8.3	12.6	11.7	52	4.9	0.2	1.0	1.1	1.8	861
16△	2013-05-16 21:36	M1.3	11748	−1	69	07	1.8	8.9	16.9	25.0	85	5.0	1.5	1.0	1.8	2.5	⋯
17	2013-05-31 19:52	M1.0	11760	−1	37	03	0.3	7.0	16.4	37.6	95	2.8	0.3	1.0	1.3	2.7	388
18	2013-08-17 18:49	M1.4	11818	1	108	20	2.2	10.1	24.1	61.9	89	6.3	1.2	1.1	1.9	4.9	1202
19△	2013-12-28 17:53	C9.3	11936	−1	112	06	1.2	8.2	17.9	25.5	37	2.1	0.7	1.0	2.8	2.8	⋯
20	2014-01-07 18:04	X1.2	11944	1	355	50	3.7	9.6	10.1	21.8	77	9.4	2.2	1.1	1.1	1.7	1830
21	2014-01-31 15:32	M1.1	11968	−1	105	07	0.3	8.3	11.3	8.8	123	5.5	0.3	1.0	0.9	1.7	462
22	2014-02-01 07:14	M3.0	11967	−1	336	23	9.6	14.4	23.6	34.4	133	7.2	7.1	1.1	1.7	1.0	⋯
23	2014-02-12 03:52	M3.7	11974	−1	196	32	6.8	8.6	17.0	24.9	69	11.8	4.5	1.0	1.3	1.2	373
24	2014-03-20 03:42	M1.7	12010	1	103	07	1.6	8.1	14.5	15.0	83	3.5	1.5	1.0	0.8	1.9	740
25	2014-08-01 17:55	M1.5	12127	1	162	21	0.6	9.3	12.5	12.0	69	6.0	0.5	1.0	1	1.1	789
26	2014-08-25 14:46	M2.0	12146	−1	114	13	2.4	11.1	25.9	38.2	59	5.9	1.7	1.1	2.4	1.5	555
27	2014-08-25 20:06	M3.9	12146	−1	106	13	2.2	9.8	28.0	35.0	74	6.1	1.9	1.1	2.0	2.0	711
28	2014-09-08 23:12	M4.5	12158	−1	140	28	3.7	13.1	21.5	25.6	65	6.3	2.8	1.2	1.4	1.3	920
29+	2014-09-10 17:21	X1.6	12158	−1	154	60	2.7	13.1	16.5	24.6	30	9.6	1.7	1.2	1.6	1.6	1267
30	2014-09-28 02:39	M5.1	12173	−1	262	21	2.9	10.4	17.5	21.2	137	8.0	2.8	1.0	1.8	1.0	215
31△	2014-10-22 14:02	X1.6	12192	−1	614	70	15.9	13.2	21.3	20.2	192	17.4	10.8	1.0	1.2	0.9	⋯
32△	2014-10-24 21:07	X3.1	12192	−1	661	102	12.5	13.2	18.2	19.5	209	29.3	9.2	1.0	1.1	0.8	⋯
33△	2014-10-25 16:55	X1.0	12192	−1	632	77	14.8	13.0	21.5	20.1	350	24.0	11.0	1.0	1.2	0.8	⋯
34△	2014-12-17 00:57	M1.5	12242	1	273	10	2.4	11.1	20.5	24.4	147	3.4	2.0	1.0	1.8	1.0	⋯
35	2014-12-17 04:25	M8.7	12242	1	290	34	2.5	12.5	18.1	27.4	89	6.1	2.0	1.1	1.9	0.9	587
36	2014-12-18 21:41	M6.9	12241	1	227	37	4.4	9.9	18.2	33.4	62	9.0	2.8	1.2	2.6	1.3	1195
37	2014-12-20 00:11	X1.8	12242	1	354	80	7.1	11.5	19.9	25.5	161	30.5	5.1	1.1	1.2	1.7	841
38	2015-11-04 13:31	M3.7	12443	1	206	33	0.9	7.0	7.8	20.4	40	6.1	0.7	1.0	1.2	0.7	578
39	2015-11-09 12:49	M3.9	12449	1	73	17	0.7	8.4	15.6	11.3	125	9.5	0.5	1.0	0.9	0.9	1041

Note. Here H, Φ, $\overline{\alpha}$, $I_{z,u}$, $|DC/RC|$, and V_{CME} refer to AR handedness, magnetic flux, mean magnetic shear, total and net currents, and CME speed, respectively. Triangles mark confined events. A plus sign marks an example event (Section 3.1). See Section 3 for details.

(This table is available in machine-readable form.)

properties before the flare and (2) a sequence of AIA 1600 Å images of $dt_{1600} = 24$ s cadence and $ds_{1600} = 0''61$ angular resolution, $I_{1600}(x, y, t)$, to find areas that have been swept up by flare ribbons during the course of the flare (i.e., cumulative ribbon masks; see Kazachenko et al. 2017). For the magnetic field, we use a full-disk vector magnetogram data set from the 135 s series (Sun et al. 2017; hmi.B_135S). To disambiguate the azimuth orientation of the magnetic field, we use the radial acute disambiguation method (Hoeksema et al. 2014). We process the UV 1600 Å images in IDL using the aia_prep.pro SolarSoft package and coalign the AIA image sequence in time with the first frame. We use aia_prep.pro to align the HMI vector magnetic field maps with the AIA image sequence. In all magnetic field calculations, we set to zero the components of the vector magnetic field $\boldsymbol{B}$, where $|B_z| < 20$ G. This noise threshold is chosen experimentally to remove areas outside the AR (Hoeksema et al. 2014). For finding PILs, we first smooth the input magnetic field with a Gaussian function with a window size of 2 pixels, then isolate areas where the vertical magnetic field $|B_z| > 200$ G and finally dilate areas of positive and negative flux with a window size of 8 pixels. This procedure results in PILs that are roughly 8 AIA pixels or ≈3500 km wide. We notice that some of the derived PILs
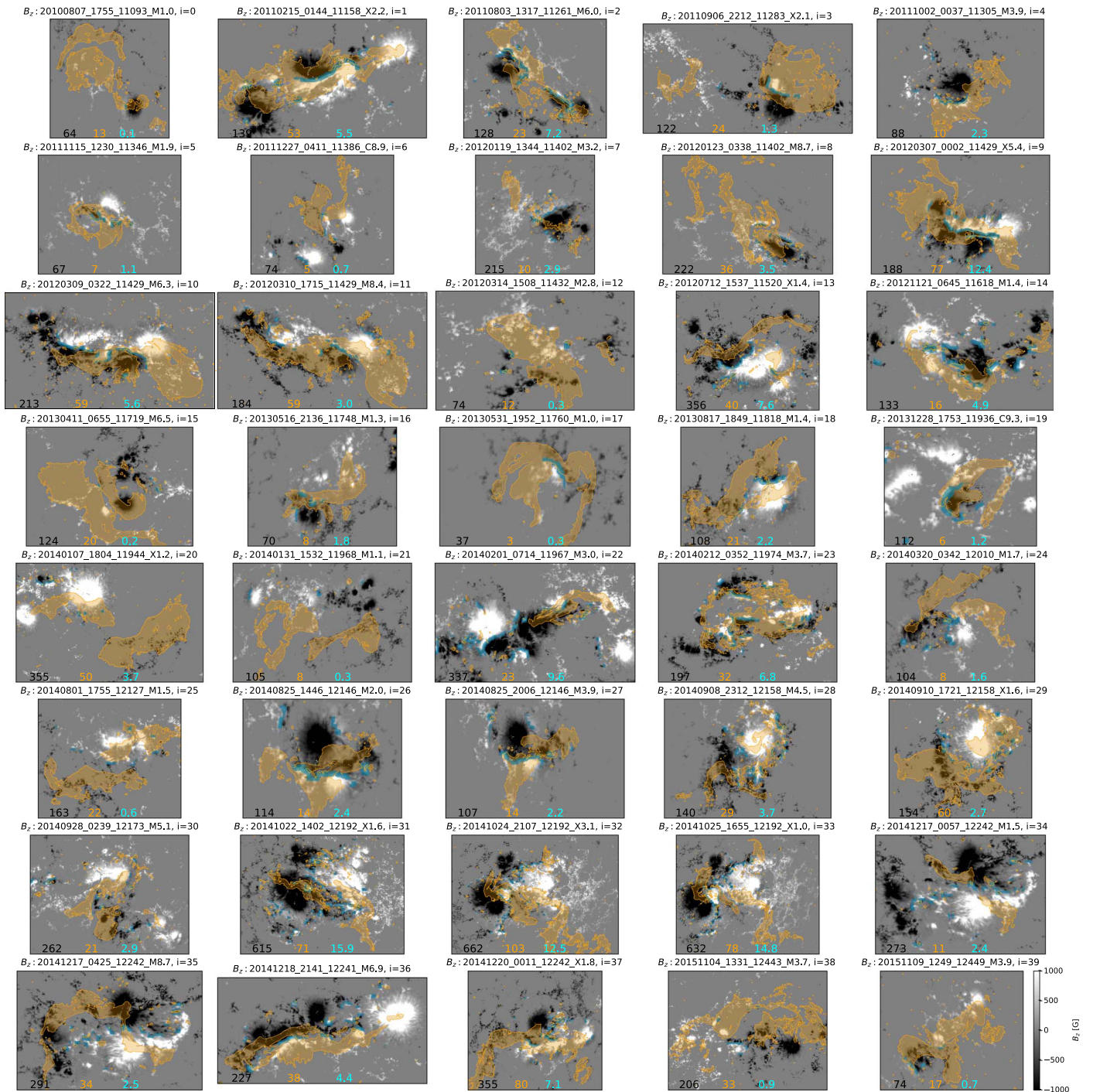
Figure 2. Vertical magnetic field maps, B_z, for 40 events from the `FlareMagDB` database. Cyan shows PIL areas. Orange shows cumulative ribbon areas. Labels above each figure combine the event's index in the database, the flare start time, the NOAA AR number, and the GOES peak X-ray flux. The "eruptive/confined" label indicates whether the event is eruptive or confined. Black, orange, and cyan numbers indicate the total magnetic flux within the AR, ribbon, and PIL areas, respectively, in units of 10^{20} Mx (see column Φ in Table 1). Here and in Figures 11 and 12, we zoom into the ROI's field of view to highlight the AR structure.

are not directly related to the flaring regions; there are few false PILs in the isolated-sunspots penumbra and PILs that lie away from the flares. However, the areas and fluxes of these PILs do not contribute significant amounts of flux in our analysis, and we thus do not exclude them. To account for noise in the weak transverse component of $\boldsymbol{B}$, we set $B_h = (B_x, B_y) = 0$, where $|B_h| < 200$ G. We define the AR region of interest (ROI) as an 800×800 pixel, or $390'' \times 390''$, rectangle centered on the AR. We chose a rectangle big enough to include the AR as a whole and small

enough to exclude neighboring ARs. We derive the coordinates of the AR center from the Heliophysics Event Catalogue maintained by the INAF–Trieste Astronomical Observatory.

2.2. Methods: Analyzed Physical Variables

We use HMI/SDO photospheric vector magnetic field maps in Cartesian coordinates, $\boldsymbol{B}(x, y) = (B_x, B_y, B_z)(x, y)$, to find the following preflare magnetic field properties: the potential
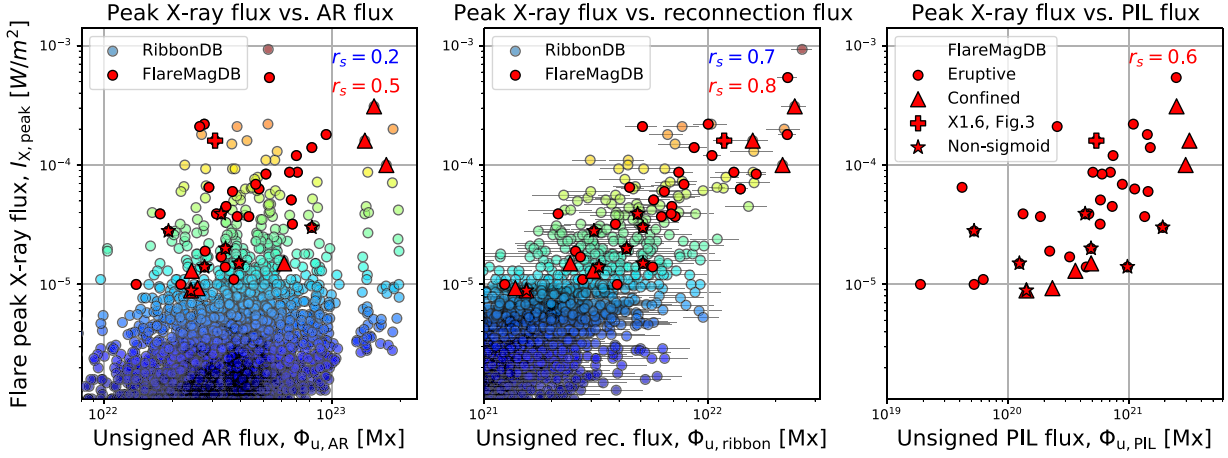
Figure 3. Comparison of `FlareMagDB` (red) vs. `RibbonDB` (rainbow) flare samples: scatter plots of peak X-ray flux vs. unsigned preflare AR magnetic flux (left), flare reconnection flux (middle), and flux within the PIL (right). The rainbow of colors shows the peak X-ray fluxes of events from the `RibbonDB` database; it varies from blue for C-class flares to orange for X-class flares. Red shows a subset of 40 `FlareMagDB` events. A plus sign indicates the example X1.6 event in AR 12158 (see Section 3.1); triangles show seven non-CME events. Stars show events that do not exhibit sigmoidal structure in extreme-ultraviolet images. See Section 2.

component of the magnetic field, $\boldsymbol{B}^p = (B_x^p, B_y^p, B_z)$; the magnetic shear, $\alpha(x, y)$ (Gosain & Venkatakrishnan 2010; Wang et al. 2017; Petrie 2019); and the vertical electric current density, $J_z(x, y)$ (Liu et al. 2017):

$$\alpha(x, y) = |B| \cos^{-1}\left(\frac{\boldsymbol{B} \cdot \boldsymbol{B}^p}{B B^p}\right) = |B|\theta, \qquad (1)$$

$$J_z(x, y) = \frac{1}{\mu_0} \nabla \times B_h = \frac{1}{\mu_0}\left(\frac{\partial B_y}{\partial x} - \frac{\partial B_x}{\partial y}\right). \qquad (2)$$

To calculate the potential field $\boldsymbol{B}^p$, we used the poloidal–toroidal decomposition of the photospheric vector magnetic field (see Appendix A in Fisher et al. 2010).

From the above quantities, we find the following area-integrated physical quantities: the unsigned and average of the positive and negative magnetic fluxes (Φ_u and Φ), the total area (S), the mean shear ($\bar{\alpha}$), and the unsigned vertical current ($I_{z,u}$):

$$\Phi_u = \int |B_z| \, dS, \quad S = \int dS, \qquad (3)$$

$$\Phi = \frac{\left|\int_{B_z>0} B_z \, dS\right| + \left|\int_{B_z<0} B_z \, dS\right|}{2} = \frac{|\Phi_+| + |\Phi_-|}{2}, \qquad (4)$$

$$\bar{\alpha} = \frac{\frac{\int_{B_z>0} \alpha \, dS}{S_+} + \frac{\int_{B_z<0} \alpha \, dS}{S_-}}{2} = \frac{\bar{\alpha}_+ + \bar{\alpha}_-}{2}, \qquad (5)$$

$$I_{z,u} = \frac{\int_{B_z>0} |J_z| \, dS + \int_{B_z<0} |J_z| \, dS}{2} = \frac{|I_{z,u+}| + |I_{z,u-}|}{2}, \qquad (6)$$

where dS is the area of integration and the plus and minus subscripts refer to integration over positive and negative polarities, respectively. To describe the physical quantities within the PIL, ribbon, and AR areas, we separately integrate over three areas of interest (dS): the area of the AR ($|B_z| > 20\,\mathrm{G}$), the area swept by the flare ribbons (rbn; $|B_z| > 20\,\mathrm{G}$), and the area within the magnetic PIL vicinity. We only consider areas where $|B_h| > 200\,\mathrm{G}$ to calculate $\bar{\alpha}$ and $I_{z,u}$.

In addition, to describe the fraction of the AR undergoing magnetic reconnection, we use the percentage of the ribbon-to-AR magnetic fluxes as first described in Kazachenko et al. (2017):

$$R_\Phi = \frac{\Phi_{\mathrm{ribbon}}}{\Phi_{\mathrm{AR}}} \times 100\%. \qquad (7)$$

To estimate the net current, we follow the steps below. We first integrate the J_z values of different signs in each polarity separately and compute the direct (DC) and return (RC) currents in each polarity (Liu et al. 2017; Schmieder & Aulanier 2018). To associate the correct sign of J_z to the DC (and hence to the RC), we find the dominant sign, or handedness, of helicity, H, of the AR as a whole. To define handedness, we use the orientation of the coronal loops from the coronal images relative to the field orientation of the AR from the magnetogram. Knowing the correct sign for DC (and RC), we then calculate DC and RC in positive and negative polarities, ($|DC|^+$ and $|RC|^+$) and ($|DC|^-$ and $|RC|^-$), respectively. For a right-handed AR with positive helicity ($H > 0$),

$$DC^+ = \int_{B_z>0,J_z>0} J_z \, dS, \quad RC^+ = \int_{B_z>0,J_z<0} J_z \, dS, \qquad (8)$$

$$DC^- = \int_{B_z<0,J_z<0} J_z \, dS, \quad RC^- = \int_{B_z<0,J_z>0} J_z \, dS. \qquad (9)$$

For a left-handed AR with negative helicity ($H < 0$),

$$DC^+ = \int_{B_z>0,J_z<0} J_z \, dS, \quad RC^+ = \int_{B_z>0,J_z>0} J_z \, dS, \qquad (10)$$

$$DC^- = \int_{B_z<0,J_z>0} J_z \, dS, \quad RC^- = \int_{B_z<0,J_z<0} J_z \, dS. \qquad (11)$$

From the above DCs and RCs in positive and negative polarities, we determine the net current (or an inverse of the neutralization ratio defined in Dalmasse et al. 2015):

$$\left|\frac{DC}{RC}\right| = \frac{\frac{|DC^+|}{|RC^+|} + \frac{|DC^-|}{|RC^-|}}{2}. \qquad (12)$$

Here $\left|\frac{DC}{RC}\right|$ describes current neutralization within the ROI, an AR as a whole, or reconnected field lines connecting flare ribbons.

To describe the CMEs associated with the eruptive events in `FlareMagDB`, we include CME speeds from the Yashiro et al. (2006) catalog.

2.3. Methods: Uncertainties

To estimate the uncertainties in the observed quantities in Equations (4)–(12), we calculate their differences within positive and negative magnetic polarities. Since, for an isolated AR, opposite polarities correspond to the footpoints of a single magnetic flux system, estimates within opposite polarities should be equal within the observational errors.[8] Adopting this hypothesis, we define the error proxies for signed magnetic fluxes, mean shears, total vertical currents, and net currents in the following way:

$$\Delta\Phi = \frac{|\Phi_+| - |\Phi_-|}{2}, \quad \Delta\bar{\alpha} = \frac{|\bar{\alpha}_+| - |\bar{\alpha}_-|}{2}, \quad (13)$$

$$\Delta I_z = \frac{|I_{z,u+}| - |I_{z,u-}|}{2}, \quad \Delta\left|\frac{DC}{RC}\right| = \frac{\frac{|DC^+|}{|RC^+|} - \frac{|DC^-|}{|RC^-|}}{2}. \quad (14)$$

From the way we construct these metrics, we expect that for ideal measurements, these error proxies should be zero.

2.4. Statistical Analysis

To quantitatively describe the relationship between different properties of flares and ARs, e.g., $\mathbb{X}$ and $\mathbb{Y}$, we use the Spearman ranking correlation coefficient, $r_s(\mathbb{X}, \mathbb{Y})$ (see Figure 5). Unlike the Pearson correlation coefficient, which is used to measure the linear relationship between variables—and therefore is not optimal for nonlinearly related variables—the Spearman rank correlation provides a measure of the monotonic relationship between variables. We describe the qualitative strength of the correlation using the following guide for the absolute value of r_s (Kazachenko et al. 2017): $r_s \in [0.2, 0.39]$—weak, $r_s \in [0.4, 0.59]$—moderate, $r_s \in [0.6, 0.79]$—strong, and $r_s \in [0.8, 1.0]$—very strong. When the correlation coefficient is moderate or greater ($r_s(\mathbb{X}, \mathbb{Y}) > 0.4$), we fit the relationship between $\mathbb{X}$ and $\mathbb{Y}$ with a power-law function,

$$\mathbb{Y} = a\mathbb{X}^b. \quad (15)$$

We use the Levenberg–Marquardt nonlinear least-squares minimization method to find the scaling factor a and exponent b.

3. Results: Observational Analysis of the Data Set

In this section, we first show the results of the magnetic field analysis within the PIL, ribbon, and AR areas for the example AR 12158 (Section 3.1, Figure 4). We then describe the results of the statistical analysis for 40 events of `FlareMagDB`: magnetic flux (Section 3.2), flux ratio (Section 3.3), magnetic shear (Section 3.4), and total and net currents (Section 3.5). Table 1 contains a list of all of the variables for 40 events.

Table 2 and Figure 5 show the variables' typical range and a correlation matrix of 18 `FlareMagDB` variables.

3.1. FlareMagDB Example Event: X1.6 Flare in AR 12158

Figure 4 shows an example of our analysis for one event in the `FlareMagDB` database, an X1.6 flare on 2014 September 10 in AR 12158 (event number $i = 29$ in Table 1). Four panels show vertical and horizontal magnetic field components, shear, and current density maps right before the flare. Orange contours indicate areas swept by the flare ribbon. Cyan contours show the locations of the PILs. In Table 1, we show the results of the quantitative analysis for this event (marked with a plus sign) and all other `FlareMagDB` events. From the magnetic flux analysis, we find that the AR magnetic flux is $\Phi_{AR} = 154 \times 10^{20}$ Mx, the magnetic flux swept by flare ribbons is $\Phi_{rbn} = 60 \times 10^{20}$ Mx, and the PIL magnetic flux is $\Phi_{PIL} = 2.7 \times 10^{20}$ Mx (Figure 4(a)). We find that the mean shear is largest within the PIL area gradually decreasing within the ribbon and AR areas ($\bar{\alpha}_{PIL} = 24.6 \times 10^3$ G$^\circ$ versus $\bar{\alpha}_{ribbon} = 16.5 \times 10^3$ G$^\circ$ and $\bar{\alpha}_{AR} = 13.1 \times 10^3$ G$^\circ$), which corresponds to the field being increasingly sheared as we go from the AR to the ribbon and PIL areas. In Figure 4(c), we can see this transition from the most yellow, or largest-shear areas, near the cyan PILs to bluer, i.e., smaller-shear areas, outside the ribbon and PIL contours in the AR as a whole (Figures 4(b) and (c)). As for the net vertical current that describes the current neutralization, we find that the current is nonneutralized within separate polarities, increasing from the AR to PIL areas: |DC/RC|[AR, rbn, PIL] = [1.2, 1.6, 1.6]. In Figure 4(d), we see this current imbalance as preferred current colors in opposite magnetic polarities; notice how the current is more violet within the positive ribbon (orange contour in the top right) and more green within the negative ribbon (bottom left).

3.2. FlareMagDB Statistics: Magnetic Flux

Figure 2 shows the vertical magnetic field maps, $B_z(x, y)$, of 40 events in the `FlareMagDB` database. Does the geometry of the PIL affect where the flare ribbons of the next flare would be? Does a stronger PIL necessarily mean that the flare ribbons of the next flare would lie close to the PIL? According to the standard flare model, ribbons should never cross PILs and should lie on both sides of the PIL at a distance defined by the reconnection process and the structure of the preflare coronal magnetic field. We examine the spatial distribution of the cyan and orange contours showing the PIL and ribbon areas (see Figure 2). We find that the ribbons and PIL masks generally sample different parts of the ARs. For example, for the 10 strongest flares, X-class and above, only three X-class flares have ribbons lying close to strong PIL areas ($i = 1, 3, 9$). In the other seven X-class flares, the ribbons lie away from strong PIL areas ($i = 13, 20, 29, 31, 32, 33, 37$). From this comparison, we conclude that while large amounts of near-PIL flux indicate that a large flare is more likely, the morphology of PILs has almost no bearing on the morphology of flare ribbons. We then use these $B_z(x, y)$ maps to find unsigned and averaged between opposite polarities vertical magnetic fluxes, Φ_u and Φ (Equations (3)–(4)), for each event within the AR, ribbon, and PIL areas (see contours).

Figure 3 shows scatter plots of preflare unsigned magnetic fluxes, Φ_u (see Equation (3)), within the AR, reconnection, and PIL areas versus peak X-ray flux for each event in the

---

[8] We note that our shear parameter does not obey any conservation principle. Also, our PIL algorithm does not enforce balance in either flux or current. Nonetheless, we do not expect substantial imbalances in these quantities, so it is plausible to use excursions from zero in these quantities to indicate large uncertainties, perhaps arising from systematic effects.
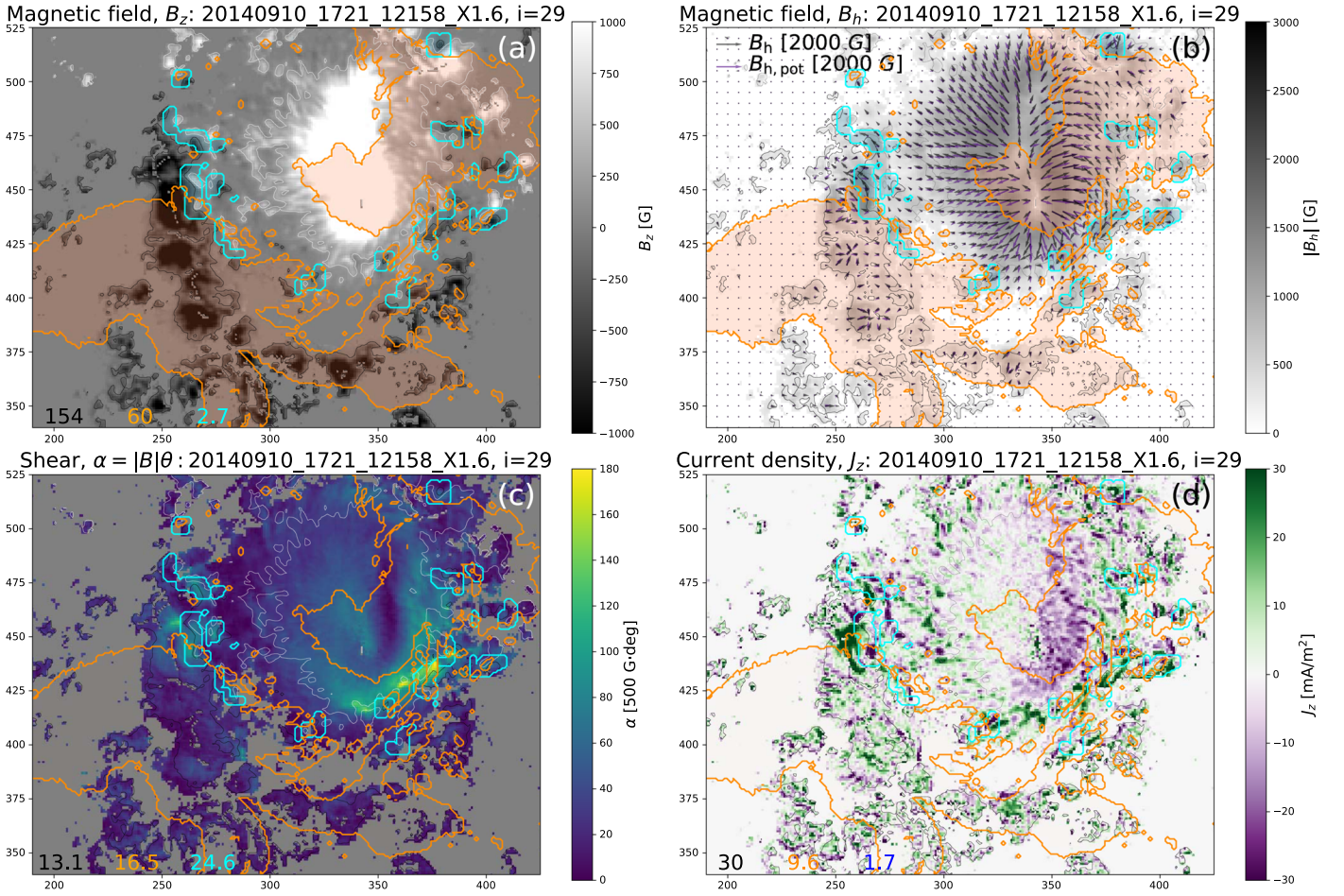
Figure 4. Example of an X1.6 flare on 2014 September 10 in AR 12158 from the `FlareMagDB` database: vertical and horizontal components of the magnetic field, magnetic shear, and the vertical current density before the flare. Orange and blue contours outline ribbon and PIL areas, respectively. Black and blue arrows show observed and potential components of the horizontal magnetic field. See Section 3.1.

Table 2
Typical Range of AR, Flare Ribbon, and PIL Properties, $\mathbb{X}$, for 40 Events of the `FlareMagDB` Database and ARMS Simulation

Quantity $\mathbb{X}$	Observations (`FlareMagDB`) Typical Range, $\mathbb{X}[P_{20}, P_{80}]$			Simulations (ARMS) $\mathbb{X}_{\mathrm{ARMS}}$		
	AR	Ribbon	PIL	AR	Ribbon	PIL
Magnetic flux, Φ [10^{20} Mx]	[100, 276]	[10, 54]	[0.9, 6.9]	41	18	0.3
Reconnection flux fraction, R_Φ [%]	...	[8.3, 20.1]	...	...	43	...
Mean magnetic shear, $\bar{\alpha}$ [10^3 G°]	[8.2, 12.9]	[14.2, 21.7]	[18.3, 34.9]	0.06	0.13	0.17
Total current, $I_{z,u}$ [10^{12} A]	[50, 139]	[4.7, 14]	[0.7, 4.0]	0.3	0.2	0.003
Net current, $|DC/RC|$ [−]	[1.0, 1. 16]	[1.1, 1.9]	[1.0, 2.4]	4.9	10.5	3.1

Note. Here $\mathbb{X}$ is either magnetic flux Φ, ribbon-to-AR fraction of magnetic flux R_Φ, mean magnetic shear $\bar{\alpha}$, total unsigned current $I_{z,u}$, or net current $|DC/RC|$. We describe the typical range of each quantity as the 20th–80th percentile, $\mathbb{X}[P_{20}, P_{80}]$. For more details, see Figures 6 and 7.

`FlareMagDB` database. Rainbow colors correspond to events from the 3137 flares in the `RibbonDB` catalog ($n = 3137$; Kazachenko et al. 2017). Red shows a subset of 40 `FlareMagDB` events selected in this paper. For events from `FlareMagDB`, we find a moderate correlation between the unsigned AR flux and the flare peak X-ray flux. This correlation is stronger than the correlation found for `RibbonDB`: Spearman correlation coefficient $r_s = 0.5$ for $n = 40$ versus $r_s = 0.2$ for $n = 3137$ (left panel). We also find a strong correlation between the unsigned reconnection flux and the flare peak X-ray flux: $r_s = 0.8$ for $n = 40$ versus $r_s = 0.7$ for $n = 3137$ (middle panel). We explain the difference in

correlation coefficients between a subsample of $n = 40$ events and the full sample of $n = 3137$ by the high heterogeneity of the full `RibbonDB` data set. We also note that, using the H_α data set from the Kanzelhohe Observatory instead of the AIA/ SDO observations, Tschernitz et al. (2018) found stronger correlations ($r_s = 0.9$) in agreement with our findings here. Finally, we find a strong correlation between the PIL vertical magnetic flux and the flare peak X-ray flux: $r_s = 0.6$ (right panel).

In Figure 6(a), we show AR, ribbon, and PIL magnetic fluxes averaged between opposite polarities, Φ versus the peak X-ray flux for the `FlareMagDB` alone (see Equation (4)). By

FlareMagDB: Correlation Matix

	Flux: AR	Flux: rbn	Flux: PIL	Flux Fraction	Shear: AR	Shear: rbn	Shear: PIL	TotCur: AR	TotCur: rbn	TotCur: PIL	MeanCur: AR	MeanCur: rbn	MeanCur: PIL	|DC/RC|: AR	|DC/RC|: rbn	|DC/RC|: PIL	X-ray flux	CME speed
Flux: AR	1.0	0.8	0.8	0.0	0.7	0.3	0.1	0.4	0.6	0.8	0.1	0.0	-0.4	0.1	-0.0	-0.4	0.6	0.1
Flux: rbn	0.8	1.0	0.7	0.6	0.7	0.4	0.2	0.2	0.9	0.7	0.3	-0.1	-0.4	0.3	-0.0	-0.2	0.9	0.3
Flux: PIL	0.8	0.7	1.0	0.2	0.8	0.6	0.4	0.4	0.7	1.0	0.3	0.2	-0.3	0.4	0.2	-0.1	0.6	0.0
Flux Fraction	0.0	0.6	0.2	1.0	0.3	0.2	0.3	-0.3	0.6	0.1	0.2	-0.2	-0.2	0.4	-0.0	0.1	0.5	0.6
Shear: AR	0.7	0.7	0.8	0.3	1.0	0.7	0.3	0.3	0.6	0.8	0.2	0.1	-0.4	0.3	0.1	-0.2	0.6	0.2
Shear: rbn	0.3	0.4	0.6	0.2	0.7	1.0	0.7	0.1	0.4	0.6	0.3	0.4	-0.0	0.4	0.6	0.2	0.4	0.0
Shear: PIL	0.1	0.2	0.4	0.3	0.3	0.7	1.0	-0.2	0.2	0.4	0.1	0.3	0.0	0.7	0.7	0.5	0.2	0.2
TotCur: AR	0.4	0.2	0.4	-0.3	0.3	0.1	-0.2	1.0	0.3	0.4	-0.2	-0.0	0.1	-0.4	-0.4	-0.3	0.1	-0.1
TotCur: rbn	0.6	0.9	0.7	0.6	0.6	0.4	0.2	0.3	1.0	0.7	0.2	-0.1	-0.3	0.2	-0.1	-0.1	0.8	0.3
TotCur: PIL	0.8	0.7	1.0	0.1	0.8	0.6	0.4	0.4	0.7	1.0	0.3	0.2	-0.2	0.3	0.1	-0.1	0.6	-0.0
MeanCur: AR	0.1	0.3	0.3	0.2	0.2	0.3	0.1	-0.2	0.2	0.3	1.0	0.6	-0.1	0.3	0.2	-0.1	0.2	0.0
MeanCur: rbn	0.0	-0.1	0.2	-0.2	0.1	0.4	0.3	-0.0	-0.1	0.2	0.6	1.0	0.1	0.2	0.4	-0.1	-0.0	-0.3
MeanCur: PIL	-0.4	-0.4	-0.3	-0.2	-0.4	-0.0	0.0	0.1	-0.3	-0.2	-0.1	0.1	1.0	-0.3	0.1	0.2	-0.3	-0.3
|DC/RC|: AR	0.1	0.3	0.4	0.4	0.3	0.4	0.7	-0.4	0.2	0.3	0.3	0.2	-0.3	1.0	0.5	0.4	0.3	0.4
|DC/RC|: rbn	-0.0	-0.0	0.2	-0.0	0.1	0.6	0.7	-0.4	-0.1	0.1	0.2	0.4	0.1	0.5	1.0	0.4	-0.0	-0.3
|DC/RC|: PIL	-0.4	-0.2	-0.1	0.1	-0.2	0.2	0.5	-0.3	-0.1	-0.1	-0.1	-0.1	0.2	0.4	0.4	1.0	-0.1	-0.3
X-ray flux	0.6	0.9	0.6	0.5	0.6	0.4	0.2	0.1	0.8	0.6	0.2	-0.0	-0.3	0.3	-0.0	-0.1	1.0	0.3
CME speed	0.1	0.3	0.0	0.6	0.2	0.0	0.2	-0.1	0.3	-0.0	0.0	-0.3	-0.3	0.4	-0.2	0.2	0.3	1.0

−1.00   −0.75   −0.50   −0.25   0.00   0.25   0.50   0.75   1.00

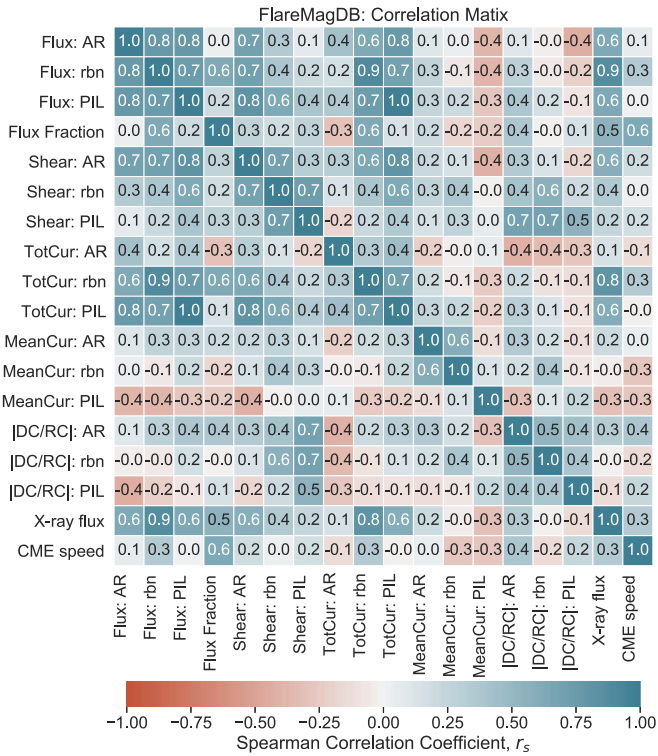Spearman Correlation Coefficient, r_s

Figure 5. FlareMagDB correlation matrix showing Spearman correlation coefficients, r_s, between variables of FlareMagDB, $\mathbb{X}$. Here $\mathbb{X}$ is either magnetic flux, ribbon-to-AR fraction of magnetic flux, mean magnetic shear, total current, mean current, net current within AR, ribbon and PIL areas, GOES peak X-ray flux, or CME speed. Colors correspond to the strength of the correlation coefficient, r_s, between each variable pair. We verbally describe the strength of the correlation using the following guide for the absolute value of r_s: $r_s = [0.2, 0.39]$—weak, $r_s = [0.4, 0.59]$—moderate, $r_s = [0.6, 0.79]$—strong, and $r_s = [0.8, 1.0]$—very strong.

definition, these averaged fluxes are around twice as small as the unsigned fluxes from Figure 3. We find that the flare size is moderately correlated with the AR magnetic flux and the strength of the PIL and very strongly correlated with the amount of reconnecting magnetic flux. In Table 2, we describe the typical range of AR, ribbon, and PIL fluxes consistent with earlier results (Kazachenko et al. 2017).

In Figure 5, we show the Spearman correlation coefficients between the AR, ribbon, and PIL fluxes and other FlareMagDB variables: the correlation matrix. We find very strong correlations ($r_s > 0.8$) between the magnetic flux and the total current within the PIL. Note that the PIL and AR fluxes have a weaker correlation with the peak X-ray flux than the ribbon reconnection flux. We discuss these relationships further in Section 5.

3.3. FlareMagDB Statistics: Reconnection Flux Fraction

In Figure 6(b), we show the fraction of the magnetic flux participating in the flare, R_Φ (see Equation (7)), versus the peak X-ray flux. We find that R_Φ has a moderate correlation with the peak X-ray flux ($r_s = 0.5$). The reconnection flux fraction has a typical range of 8.3%–20.1%, consistent with previous results (Kazachenko et al. 2017).

3.4. FlareMagDB Statistics: Magnetic Shear

Figure 11 in the Appendix shows magnetic shear maps, $\alpha(x, y)$, for all events of the database. From these maps, we find that the spatial structure of the magnetic shear varies greatly for different events. To understand these variations in a quantitative way, we use individual shear maps to find the mean magnetic shear, $\bar{\alpha}$, within the AR as a whole and the ribbon and PIL areas (see Equation (1)).

Figure 6(c) shows the mean magnetic shear versus the peak X-ray flux. We find that the mean magnetic shear in the AR, ribbon, and PIL areas is $[10, 18, 26] \times 10^3$ G° with a 20th–80th percentile of $[8.2, 12.9] \times 10^3$, $[14.2, 21.7] \times 10^3$, and $[18.3, 34.9] \times 10^3$ G°, respectively (see Table 2). In other words, as we go from the AR as a whole to the ribbon and PIL areas, the magnetic field becomes stronger and more sheared. In addition, we find that the peak X-ray flux has a strong correlation with the mean magnetic shear within the AR and weak-to-moderate correlations with the mean magnetic shear within the PIL and ribbon areas.

3.5. FlareMagDB Statistics: Vertical and Net Current

Figure 12 in the Appendix shows vertical current density maps, $J_z(x, y)$, for all events of the database. Zooming in to individual J_z images, we see that the vertical current density consists of long and short structures, or "threads" and "patches," of violet and green that correspond to positive and negative vertical currents. While we find elongated thread structures in some events, e.g., events $i = 1$ (01_20110215_0144_11158_X2.2), 22 (22_20140201_0714_11967_M3.0), and 36 (36_20141 218_2141_12241_M6.9), from our limited sample, we do not find any relationship between the presence of these structures and occurrence of large flares or CMEs (see, e.g., a non-threadlike event, 29_2014_0910_1721_12158_X1.6, where an X1.6 occurred with a CME). Instead, we find that the current density maps have all kinds of shapes of varying size that are not related to flare size or flare/CME productivity.

To quantify the global properties of J_z, we use J_z maps to compute the total unsigned vertical current, $I_{z,u}$, DC, RC, and their ratio, or net current, $|DC/RC|$ as described in Equations (6)–(12).

Figure 6(d) shows the scatter plot between the total unsigned vertical current and the peak X-ray flux before the flare within the PIL, ribbon, and AR areas. We find that the total unsigned vertical current is largest within the AR areas, decreasing gradually within the ribbon and PIL areas. This relationship is not surprising and reflects the decreasing area of integration as we go from the AR to ribbon and PIL areas. Comparing Figures 6(a) and (d), i.e., the vertical magnetic flux and total vertical current scatter plots, we see similar scattering with the peak X-ray flux. The Spearman correlation coefficient between the peak X-ray flux and the total vertical current ranges from weak for ARs to strong for the ribbon and PIL areas.

In Figure 7, we describe the imbalance of the vertical current within each magnetic polarity, the net current, in the AR, ribbon, and PIL areas and compare these to various magnetic field properties. Our objective here is to understand the cause of the net current. In Figure 7(a), we compare the $|DC/RC|$ with the peak X-ray flux. We find that the $|DC/RC|$ and the flare peak X-ray flux have a weak correlation, implying that the net current is not related to how large the next flare might be. We find that the net current is larger within PILs than within ribbons and separate AR polarities ($|\overline{DC/RC}| = [1.1, 1.5, 1.7]$ within ARs, ribbons, and PILs, respectively); i.e., the current is more nonneutralized within the ribbons' than the AR's polarities. If we look not at the separate polarities but at the AR as a whole, we find that $|DC/RC| \approx 1$; i.e., the current is neutralized.
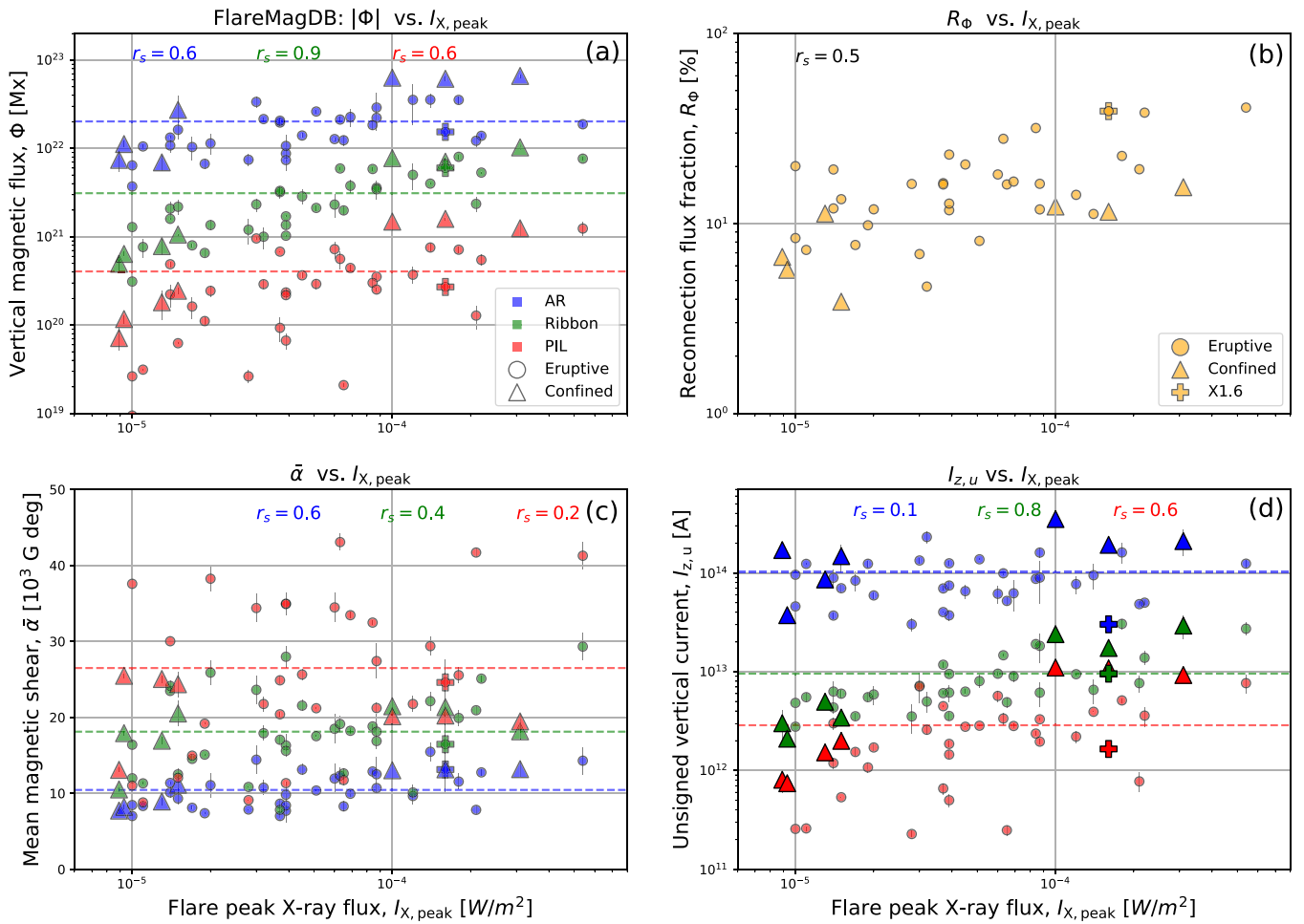
Figure 6. FlareMagDB results. Shown are magnetic field properties for 40 events of the FlareMagDB database: vertical magnetic flux (top left; Section 3.2), reconnection flux fraction (top right; Section 3.3), mean magnetic shear (bottom left; Section 3.4), and total unsigned vertical current (bottom right; Section 3.5) vs. the peak X-ray flux within the AR, ribbon, and PIL areas. The error bars correspond to error proxies as defined in Section 2.3.
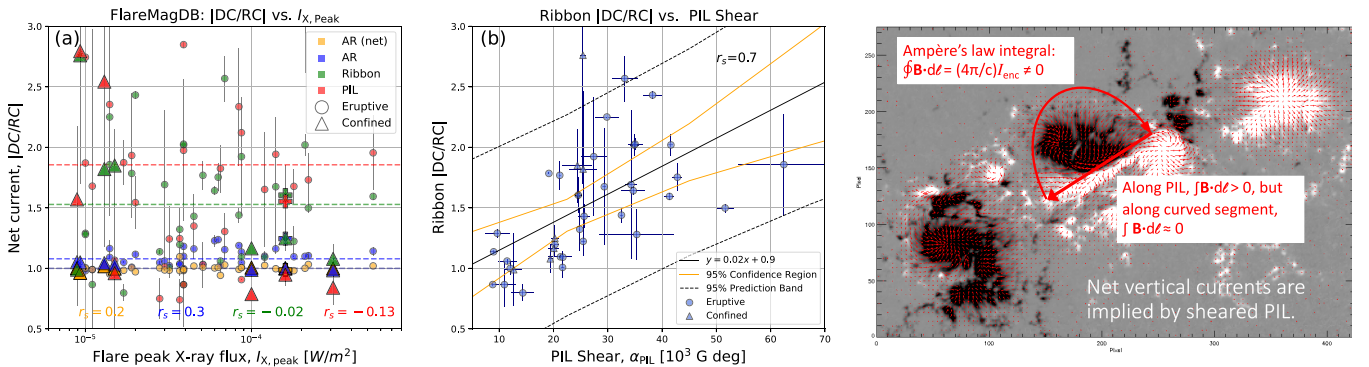

Figure 7. FlareMagDB results for the net current properties for 40 events of the FlareMagDB database. Panel (a): DC/RC vs. peak X-ray flux. Panel (b): DC/RC within ribbons vs. mean PIL shear angle. The error bars correspond to error proxies as defined in Section 2.3. Right panel: explanation of the scaling law in panel (b) between the net current and shear at the PIL as a consequence of Ampère's law. See Section 3.5.

To understand the cause of the net current, in Figure 7(b), we compare the preflare mean shear with the net current within the flare ribbons. We find a strong correlation between the net current within the ribbons and the mean shear within the PIL. Using a linear function, we find the $0.02 + 0.9$ relationship between the two and a Spearman correlation coefficient of 0.7. We find a similar relationship between the AR net current and the PIL shear, with a slightly weaker correlation coefficient.

What does this relationship imply? It implies that the net current is a manifestation of the magnetic shear at the PIL.

3.6. FlareMagDB Statistics: Confined versus Eruptive Events

We analyze the magnetic field properties of seven confined events that did not cause CMEs (marked with triangles in Figures 6 and 7) and compare them with 33 eruptive events that
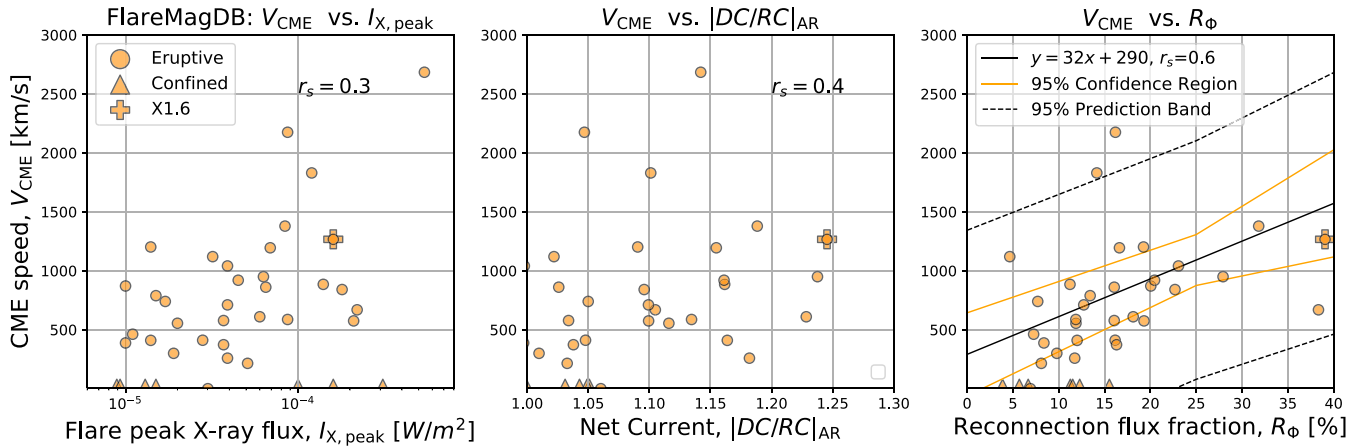
Figure 8. `FlareMagDB` results for CME speeds vs. highest-correlated flare magnetic properties, peak X-ray flux, AR net current, and reconnection flux fraction for 33 eruptive (circles) and seven confined (triangles) flares of the `FlareMagDB` database. See Section 3.6.

caused CMEs (marked with circles). Seven confined events originated in five ARs, including three X-class flares, X3.1, X1.6, and X1.0, originating in AR 12192 (Sun et al. 2015).

Comparing confined versus eruptive events, we find several differences in their magnetic field properties. First, we find that for flares within a certain peak X-ray class range, confined events have larger PIL magnetic fluxes than eruptive events (Figure 6(a)). Second, we find that confined events have a smaller PIL shear and ribbon net current than eruptive events (see triangles versus circles). Third, we find that the reconnection flux fraction, R_Φ, tends to be smaller for confined events than for eruptive events (Figure 6(b)). If we look at eruptive events alone, we find that their reconnection flux fractions strongly correlate with the CME speeds, $r_s(r_\Phi, v_{CME}) = 0.6$. In fact, among all `FlareMagDB` variables, it is the reconnection flux fraction that has the strongest correlation with the CME speed. In Figure 8, we plot the CME speed versus the `FlareMagDB` variables that have the highest correlation coefficients with the CME speed, peak X-ray flux, AR net current, and reconnection flux fraction. To summarize, we find that while the PIL shear and net current have a weak-to-moderate correlation with the CME speed, the reconnection flux fraction has a strong correlation with the CME speed; i.e., the properties of the field of the flux rope play a smaller role in the CME speed that the properties of the flux rope relative to the overlying field.

We note that our analysis of field properties within confined and eruptive events is based on 33 eruptive and only seven confined events. Analysis of a larger data sample with equal numbers of confined and eruptive events would be necessary to draw more certain conclusions.

4. Results: 3D MHD ARMS Simulations

To provide theoretical ground for our observational findings, here we present the same observational analysis of the results of a 3D MHD simulation of an idealized magnetic breakout CME (Antiochos et al. 1999; Lynch et al. 2008) that forms a large-scale posteruption arcade below an energetic flux rope eruption. We note that, while the simulation's AR magnetic flux is similar to a flux of the medium AR, the mean magnetic field strengths (and AR sizes) are about 100 times smaller (larger) in the simulations than observed. Using the scaling law between the reconnection flux and the peak X-ray flux, we

Table 3
ARMS Initial Magnetic Field Point Dipole Parameters

i	M_i (G)	R_i ($R_\odot$)	$r_{i,0}$ ($r/R_\odot$, θ, ϕ)	m_i ($\hat{r}$, $\hat{\theta}$, $\hat{\phi}$)
1	1.00	1.0	(0, 0, 0)	(0, 1, 0)
2	0.08	1.0	(0.80, 0.45π, −0.025π)	(0, 1, 0)
3	0.08	1.0	(0.80, 0.45π, +0.025π)	(0, 1, 0)
4	0.10	0.33	(0.95, 0.45π, 0)	(0, 1, 0)
5	0.10	0.33	(0.95, 0.45π, −0.010π)	(0, 1, 0)
6	0.10	0.33	(0.95, 0.45π, +0.010π)	(0, 1, 0)

conclude that the simulation's reconnection flux corresponds to an M1.0-class flare.

4.1. Model Details and Initial Conditions

The 3D MHD simulation was performed with ARMS (DeVore & Antiochos 2008). The simulation is a left-handed Lynch et al. (2009) configuration energized with a pair of idealized shearing flows parallel to the AR PIL.

The magnetic field at $t = 0$ hr is initiated via a sum of point dipoles,

$$\boldsymbol{B}(\boldsymbol{r}, 0) = \sum_i M_i \left(\frac{R_i}{r_i'}\right)^3 [\, 3\boldsymbol{n}_i(\boldsymbol{n}_i \cdot \boldsymbol{m}_i) - \boldsymbol{m}_i \,], \qquad (16)$$

where $r_i' = |\boldsymbol{r} - \boldsymbol{r}_{i,0}|$, $\boldsymbol{n}_i = \boldsymbol{r}_i'/r_i'$, and each dipole has a moment magnitude M_i, location $\boldsymbol{r}_{i,0}$, and scaling factor R_i and is pointing in the $\boldsymbol{m}_i$ direction. As in Lynch et al. (2009), $i = [1, 6]$, and the parameters used here are given in Table 3.

The base pressure and temperature are given by $p_0 = 0.025$ dyn cm^{-2} and $T_0 = 1.9433 \times 10^6$ K, respectively, while the initial solar atmosphere is in hydrostatic equilibrium with $p(r) = p_0(r/R_\odot)^{-\mu}$, $T(r) = T_0(r/R_\odot)^{-1}$, $p = 2(\rho/m_p)k_B T$, and $\mu = R_\odot/H_\odot = 12.0$ is the normalized (inverse) scale height. This yields a base mass density of $\rho_0 = 7.80 \times 10^{-17}$ g cm^{-3}, corresponding to a base number density of $n_0 = 4.6634 \times 10^7$ cm^{-3}.

The computation grid is block-decomposed with an initial resolution of $5 \times 5 \times 5$ blocks covering the full domain of $r \in [1\ R_\odot, 20\ R_\odot]$, $\theta \in [0.0625\pi, 0.9375\pi]$ (latitude of $\pm 78°75$), and $\phi \in [-0.5\pi, +0.5\pi]$. Each block contains 8^3 grid cells, and we have employed four additional levels of static grid
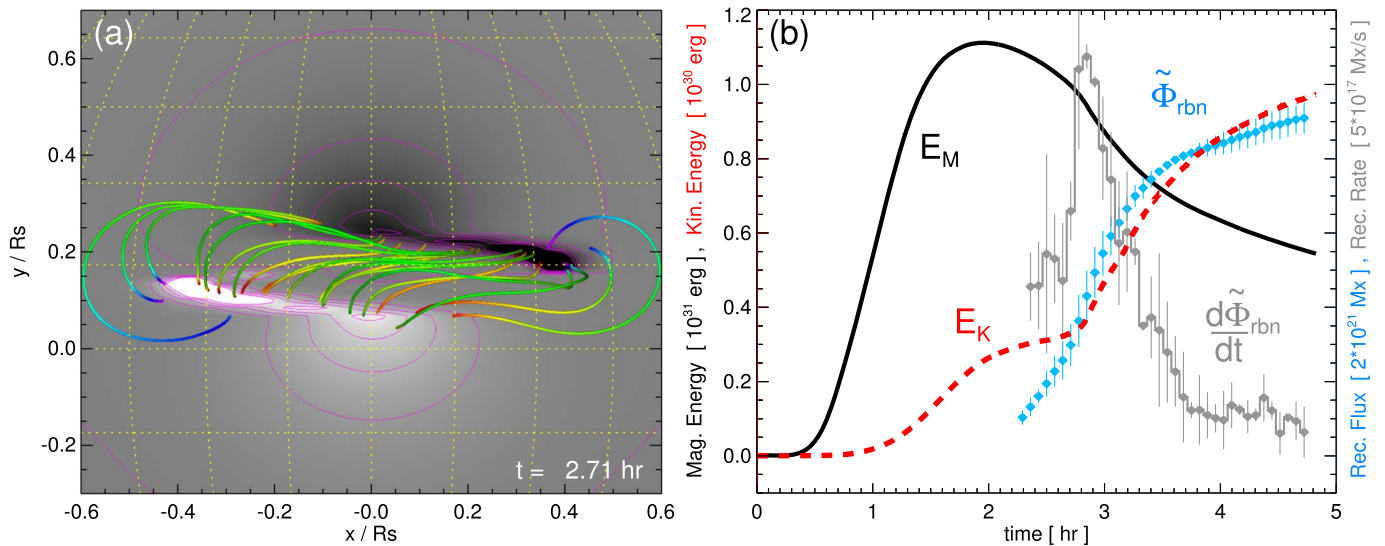
Figure 9. ARMS simulation results during the CME eruption. Panel (a): radial magnetic field on the $r = R_\odot$ lower boundary with posteruption arcade field lines at $t = 2.71$ hr. Panel (b): total magnetic, $E_M(t) - E_M(0)$, and kinetic, $E_K(t)$, energies along with total unsigned reconnection flux, Φ_{rbn}, and reconnection rate, $d\Phi_{rbn}/dt$. See Section 4.2 for details.

refinement. The highest-refined region covers $r \in [1\,R_\odot, 6\,R_\odot]$, $\theta \in [0.32\pi, 0.55\pi]$ (latitude of $[-9^\circ.0, +32^\circ.4]$), and $\phi \in [-0.18\pi, +0.18\pi]$ with an effective resolution of 320^3. Thus, the highest-refined grid cells have a $0^\circ.49 \times 0^\circ.56$ angular resolution in (θ, ϕ) and $\Delta r = 0.0188\,R_\odot$ at the lower boundary.

The energizing boundary flows impart a significant shear component (B_ϕ) to the AR as each polarity concentration is moved further apart. The form of the Lynch et al. (2009) shearing flows is

$$\mathbf{v}_h^{(\pm)} = \pm v_0 f^{(\pm)}(\theta, \phi)\left(\frac{1}{2} - \frac{1}{2}\cos\left[\frac{2\pi t}{(10^4\,\mathrm{s})}\right]\right)\hat{\phi}, \quad (17)$$

where ($\pm$) represents the flows applied to the positive and negative polarities, respectively, for the duration $t \in [0, 2.778]$ hr. The function $f^{(\pm)}(\theta, \phi)$ smoothly ramps the flow profile to zero outside of specified (θ, ϕ) ranges on either side of the PIL, described in Lynch et al. (2009). The magnitude of the shearing flows $v_0 = 65$ km s^{-1} is significantly faster than the observed photospheric velocities but below the sound speed ($c_0 \sim 180$ km s^{-1}) and extremely sub-Alfvénic ($v_A \gtrsim 2000$ km s^{-1}) in the vicinity of the AR.

4.2. Eruption Details

The magnetic breakout model for CME initiation relies on the positive feedback process associated with reconnection at a current sheet above the source region's expanding sheared core (Antiochos et al. 1999; Lynch et al. 2008). The arcade expansion accelerates as the restraining overlying flux is transferred into the adjacent arcades of the AR multipolar flux system. Reconnection at the breakout current sheet drives the initial stages of the eruption and leads to the transition from slow quasi-ideal evolution to a driven, runaway configuration that forms a vertical current sheet below the expanding sheared field core. This current sheet thins and elongates with continued expansion and, with the onset of the fast CSHKP eruptive flare reconnection, ushers in the explosive acceleration phase of the CME eruption (e.g., DeVore

& Antiochos 2008; Karpen et al. 2012; Lynch & Edmondson 2013; Dahlin et al. 2019; Wyper et al. 2021).

Figure 9 shows a snapshot of the simulation results during the CME eruption. Figure 9(a) shows the field lines of the posteruption flare arcade in the very beginning of the eruption ($t = 2.71$ hr), and Figure 9(b) shows the temporal evolution of the total magnetic energy, kinetic energy, flare reconnection flux, and reconnection rate. To focus on changes of the magnetic energy during the eruption, we have set the magnetic energy at $t = 0$ to zero: $E_M(t = 0) = 0$. The total amount of released magnetic energy, i.e., the E_M decrease from 2 to 5 hr, is $\Delta E_M \sim 6 \times 10^{30}$ erg, which roughly corresponds to the change in the free magnetic energy. The kinetic energy exhibits two stages of evolution. During the initial stage from 1 to 2.6 hr, the kinetic energy E_K increases slowly, corresponding to a slow quasi-ideal rise of the sheared core before the onset of flare reconnection. This expansion is initially caused by the force imbalance (magnetic pressure gradient) introduced with the sheared field component. During the second runaway stage, from 2.6 to 5 hr, E_K increases much more rapidly, corresponding to the start of the breakout reconnection. Once the flare reconnection starts, it becomes the dominant process driving the entire subsequent evolution of the CME eruption (Karpen et al. 2012). By the end of the flare at $t = 5$ hr, the kinetic energy reaches a maximum of $E_K \sim 10^{30}$ erg, and the cumulative unsigned reconnection flux reaches $\Phi_{rbn} \sim 1.8 \times 10^{21}$ Mx. The maximum reconnection rate is $d\Phi_{rbn}/dt \sim 5.5 \times 10^{17}$ Mx s^{-1} at $t = 2.85$ hr. The total fraction of the AR flux that participated in the flare is 43% (Table 2).

4.3. Magnetic Field and Electric Current Properties in the AR, PIL, and Flare Ribbon Regions

To apply the observational analysis framework to the simulation results, we first project the spherical magnetic field components into a Cartesian coordinate system, where (x, y) represents the plane of the sky (horizontal components) and z comes out of the page toward the observer (vertical component). Next, we interpolate the simulation values onto a uniform 600×500 array corresponding to the area shown in
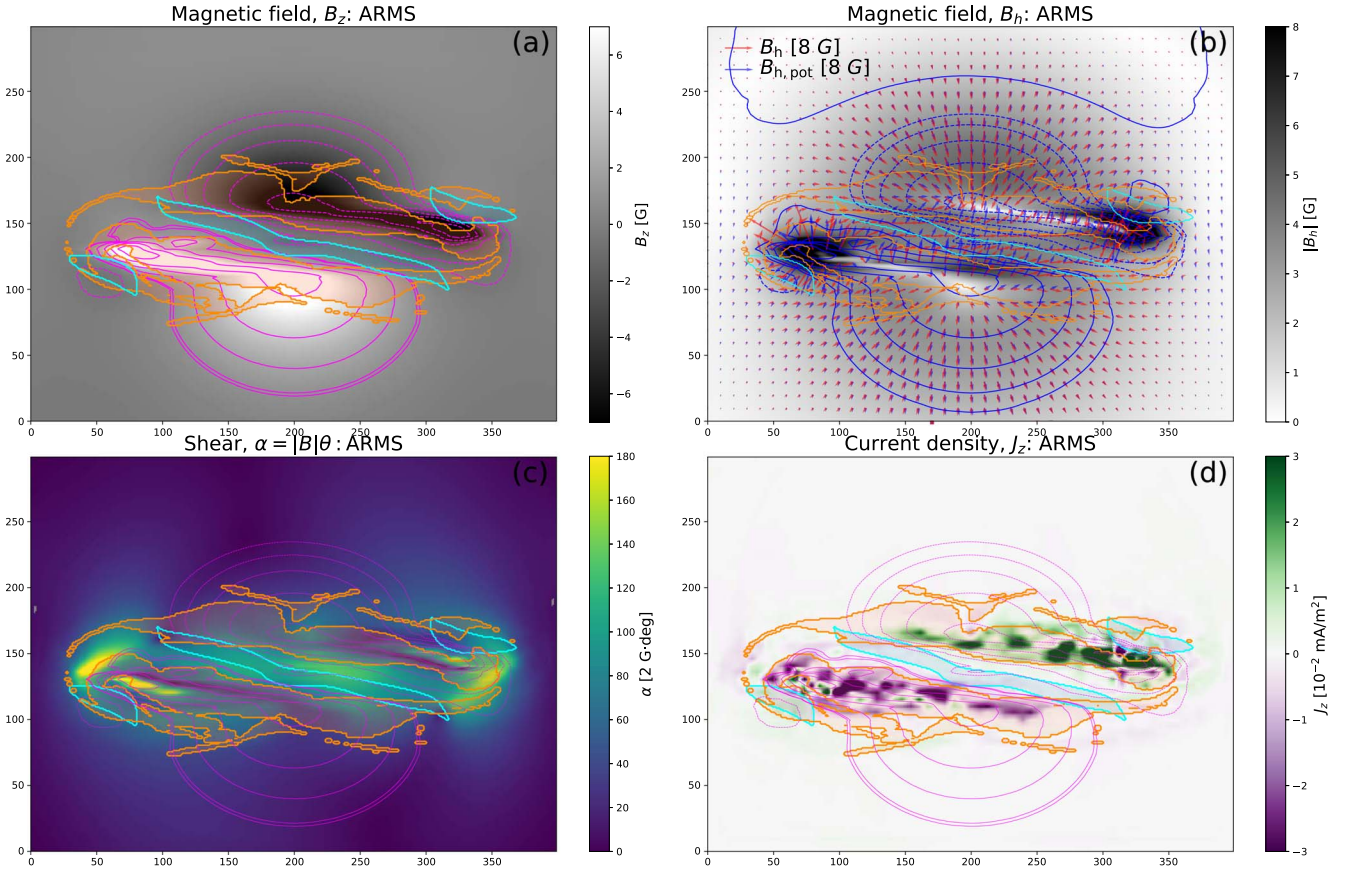
Figure 10. ARMS MHD quantities on the $r = R_\odot$ lower boundary analogous to those presented for an observed X1.6 flare in Figure 4. Panel (a): vertical field B_z. Panel (b): magnitude of the horizontal magnetic field and vector directions of the total and potential components (arrows). Panel (c): distribution of magnetic shear $\alpha(x, y)$. Panel (d): vertical current density $J_z(x, y)$. In each panel, the total flare ribbon area during the eruption is denoted as the orange shaded region, while the cyan shaded region indicates the AR PIL. See Section 4.3 for details.

Figure 9(a), i.e., $x \in [-0.6 \ R_\odot, +0.6 \ R_\odot]$, $y \in [-0.25 \ R_\odot, +0.75 \ R_\odot]$. This yields a pixel area $dA_{ij} = \Delta x \Delta y = 1.96 \times 10^{16}$ cm^2. From this data set, we calculate the magnetic shear $\alpha(x, y)$, vertical current density $J_z(x, y)$, and their respective averages over the regions of interest defined in Section 2.2.

Figure 10 shows the ARMS simulation version of Figure 4 at $t = 2.57$ hr, right before the onset of the fast eruptive flare reconnection. Figures 10(a) and (b) show the vertical and horizontal field components with the cumulative ribbon and PIL areas over the flare duration denoted as the orange and cyan shading, respectively. Here the ribbon areas are calculated from a field line length proxy, as in Lynch et al. (2019, 2021). Figure 10(c) shows the distribution of shear, and Figure 10(d) shows the distribution of the vertical current density.

Table 2 shows a comparison of observed values from FlareMagDB with ARMS. The mean magnetic flux in each region is $\Phi(AR, rbn, PIL) = [4.1, 1.8, 0.03] \times 10^{21}$ Mx. The mean shear in each region is $\overline{\alpha}(AR, rbn, PIL) = [63, 129, 169] \times (G°)$. The total unsigned vertical current in each region is $I_{z,u}(AR, rbn, PIL) = [2.7, 2.1, 0.03] \times 10^{11}$ A. The net current in each region is $|DC/RC|(AR, rbn, PIL) = (4.9, 10.5, 3.1)$. Comparing these values with observations, the ARMS magnetic fluxes correspond to a medium-sized flare in a medium-sized AR. For example, an M1.0-class flare in a sigmoidal AR ($i = 0$) of FlareMagDB has very similar AR, ribbon, and PIL magnetic fluxes. The size of the ARMS AR is much larger than any observed case; therefore, the magnetic

fields are much weaker. Since the magnetic fields are much weaker, the ARMS magnetic shears (which are a product of the magnetic field magnitude and the shear angle, θ) and total currents are much smaller than the observed ones. We also find that the ARMS AR has very weak RCs, resulting in large net currents, which vary from 5 for a single polarity to 10.5 within a flare ribbon. For comparison, the observed ARs have smaller net currents ranging from 1 to 3; i.e., the RCs in the observations are stronger. Note that before the eruption, when we start shearing the arcade, there is DC close to the PIL and a clear RC shell separating the sheared from unsheared components along the QSL. During the eruption, the RC weakens as a result of peeling away the outer layers of the expanding flux system via breakout reconnection.

To summarize, from the ARMS analysis, we find the following. (1) Similar to observations, the simulations' mean magnetic shear increases gradually from the AR to ribbon and PIL areas. The simulations' shear values are consistent with the observed ones, given a 100 times scaling relation between mean magnetic fields. (2) Similar to observations, the vertical electric currents within individual polarities are highly nonneutralized, with the largest net currents located within areas involved in the eruption. The simulations' net currents are ≈five times stronger than the observed values. (3) We find a close spatial relationship between the simulation's magnetic shear at the PIL and the net current, confirming the new net current–shear scaling law we find from the observations.

5. Discussion

We used HMI/SDO photospheric vector magnetic field observations in 40 flares to assemble a `FlareMagDB` database with the properties of the magnetic fields within the AR, flare ribbon, and PIL areas. We analyzed the preflare observed magnetic flux, reconnection fraction, magnetic shear, total electric current, and net current for 40 events and compared these with the flare X-ray peak flux (Figures 6 and 7) and CME speed (Figure 8). In Table 2, we summarized the variables' typical ranges and compared these with synthetic variables from an MHD ARMS eruption simulation. In the correlation matrix in Figure 5, we investigated dependencies between the variables. In this section, we describe how our results complement the existing understanding of flare magnetism.

Ribbon versus PIL morphology. We compare the spatial distribution of ribbons and PILs and find that many flares, including M5.0 and above, have ribbons lying away from the PIL. What does this imply? First, that for many events, the morphology of PILs has almost no bearing on the morphology of flare ribbons. Second, that in these events, low-lying magnetic fields that are rooted in the vicinity of the PIL area do not participate in the flare. How do these ideas fit within the contention that large near-PIL fluxes indicate that a large flare is more likely to occur (Schrijver 2007)? We explain this with the fact that the majority of events in our list, 33 out of 40, have sigmoidal coronal structure (Canfield et al. 2007; Savcheva et al. 2014). A sigmoid is a twisted flux rope embedded in a surrounding field. Savcheva et al. (2012a, 2012c) analyzed the time evolution of a sigmoid eruption and constructed a scenario for the onset of the CME in sigmoidal regions: the preexisting flux rope can develop into a CME as a consequence of reconnection at a hyperbolic flux tube under the flux rope, which increases the magnetic flux in the rope and at the same time weakens the overlying magnetic arcade holding it down. Thus, tether-cutting reconnection is needed in the slow rise phase of the eruption, and the torus instability is necessary to allow the CME eruption. On the other hand, the presence of ribbons close to the PIL indicates either the presence of a low-lying preexisting flux rope or the creation of a flux rope during the flare as a result of the reconnection of the low-lying sheared magnetic fields (Kazachenko et al. 2012). A more detailed study of flare ribbon versus PIL position and properties relative to coronal structure would be helpful to advance our understanding of flux rope formation.

Magnetic flux. From the analysis of magnetic fluxes, we find that the ribbon and PIL fluxes have a strong correlation with the AR flux, implying that large PIL and ribbon fluxes tend to occur in ARs with large magnetic fluxes. We also find that magnetic fluxes have a moderate-to-strong correlation with other magnetic field products like mean magnetic shear and the total current. Specifically, the correlation between the PIL flux and the AR shear is very strong ($r_s = 0.8$; see Figure 5). One possible scenario to explain this relationship is that as the AR evolves and gets pushed by photospheric flows, the AR field becomes more sheared, and magnetic flux piles up at the PIL due to, for example, collisional shearing (Chintzoglou et al. 2019).

We find a strong correlation between the AR, ribbon, and PIL magnetic fluxes and the peak X-ray flux ($r_s > 0.6$). While strong, the correlation between the PIL flux and the X-ray peak flux is weaker than the correlation between the PIL flux and the AR flux ($r_s = 0.6$ versus $r_s = 0.8$). In other words, while the

correlation between the PIL flux and flare size is in line with the Schrijver (2007) hypothesis that flare-productive ARs tend to have stronger PILs (see also references in Georgoulis et al. 2019), this correlation could reflect the fact that larger ARs have stronger PILs and hence host larger flares. A study of small versus large ARs with the same amount of PIL flux might be useful to find out what plays the major role in the AR flare production, the AR flux or the PIL flux. We also find a very strong correlation between the reconnection flux and the peak X-ray flux ($r_s = 0.9$), in agreement with earlier results for larger data sets (Kazachenko et al. 2017; Toriumi et al. 2017; Tschernitz et al. 2018). The power law between the two quantities agrees with the Warren & Antiochos (2004) scaling from hydrodynamic simulations of impulsively heated flare loops, proving that the soft X-ray radiation energy released during the flare comes from the free magnetic energy released during reconnection (Kazachenko et al. 2017).

Magnetic flux fractions. We find that fractions have a moderate correlation with the peak X-ray flux ($r_s = 0.5$) that is weaker than the correlation between the ribbon flux and the peak X-ray flux. This result is in agreement with Kazachenko et al. (2017; $r_s = 0.5$) and Toriumi et al. (2017). We explain this relationship as a consequence of how we calculate the fractions ($R_\Phi = \frac{\Phi_{\mathrm{ribbon}}}{\Phi_{\mathrm{AR}}} \times 100\%$) and a very strong correlation between the ribbon flux and the peak X-ray flux.

Mean magnetic shear. The amount of magnetic shear at the PIL is known to be related to the flare productivity of an AR. Here, as noted above, we find that the amount of magnetic shear within the AR is most strongly correlated with the flux at the PIL, which, in turn, is strongly correlated with the AR magnetic flux. The larger the AR, the larger the amount of shear it contains and the more flux it has at the PIL. Is the amount of shear related to the flare peak X-ray flux? From our analysis, we find that this is not the case; the mean magnetic shear has a weak-to-moderate correlation with the peak X-ray flux that is weaker than the correlation between the magnetic flux and the peak X-ray flux. For example, while the PIL flux correlates with the flare size ($r_s = 0.6$), increased PIL shear does not correlate with AR flare size ($r_s = 0.2$). We also find that this correlation decreases from ARs to ribbons and PILs. As we go further from the PIL, we get less sheared magnetic fields, consistent with the standard 3D flare model (Janvier et al. 2014; Savcheva et al. 2016). Analysis of many large flares with a large amount of PIL magnetic flux and a small amount of shear at the PIL, such as an M8.7 ($i = 8$, $\Phi_{\mathrm{PIL}} = 21.2$) or M6.5 ($i = 15$, $\Phi_{\mathrm{PIL}} = 11.7$) flare, would be interesting.

In several past investigations and ongoing work, Savcheva et al. (2015, 2016), Janvier (2016), and Karna et al. (2021) studied several of the ARs shown in Table 1, specifically, 2010 August 7 ($i = 0$), 2011 February 15 ($i = 1$), 2011 September 6 ($i = 3$), 2012 March 7 ($i = 9$), 2012 March 9 ($i = 10$), 2012 July 12 ($i = 13$), 2013 April 11 ($i = 15$), and 2014 October 22–25 ($i = 31, 32, 33$). Specifically, Savcheva et al. (2015, 2016) studied an M1.0 flare on 2010 August 7 ($i = 0$) using a magnetofrictional (MF) evolution. They found that first reconnection happens under the flux rope, turning two J-shaped field lines from the sheared arcade into an S-shaped field line that builds magnetic flux in the flux rope and produces flare field lines as a by-product. These flare field lines, which match the observed flare loops, initially lie close to the PIL and are highly sheared, carrying the remnant of the flux rope shear, and, sequentially, as the flux rope goes up in height, less and

less sheared loops form that are rooted farther and farther away from the PIL (see cartoon in Figure 1 from Savcheva et al. 2016). This scenario, using MF simulation, supports data-constrained MHD simulation by Kliem et al. (2013) and also the observed large-to-small shear transition from PIL to ribbon areas that we find here.

Spatial structure of the vertical current density. What is the spatial structure of the vertical current density, and does it have any relationship with the ability of the AR to host a CME versus a confined event? Recent works suggest that CME-eruptive ARs exhibit defined filamentary structures or ribbons in the current density maps, while CME-quiet ARs do not (see, e.g., Figure 3 of Avallone & Sun 2020). Some observed case studies and simulations suggested that a hook-shaped pattern in these filaments could be a signature of the preexisting flux rope (Janvier 2016; Schmieder & Aulanier 2018; Barczynski et al. 2020). Do we see DC ribbon pairs aligned with the PIL before an AR hosts a CME (similar to the $q = 0.8$ case in Sun & Cheung 2021)? Do these current ribbons have hook shapes? To answer this question, we examine the FlareMagDB current density maps in Figure 12. First, we notice that few of these events have a clear hook shape; i.e., while hooks might be a signature of a preexisting flux rope, hook presence is a rare phenomenon. Second, we find that while some eruptive events are associated with distinct current ribbon pairs close to the PIL, others do not have these current ribbon pairs, instead consisting of salt-and-pepper patterns of positive and negative current density. For example, AR 11158 ($i = 1$; eruptive X2.2 flare) and AR 12241 ($i = 36$; eruptive M6.9 flare) have clear current ribbon pairs, while AR 11944 ($i = 20$; eruptive X1.2 flare) does not have current ribbons. Does this mean that eruptive events that do not have current ribbons are all in situ formed flux ropes, i.e., flux ropes that were primarily formed during reconnection? Finally, we find that all seven confined events in our list do not have current ribbons. This result is consistent with earlier works and the scenario that a lack of current ribbons might be related to the absence of the preexisting flux rope and, as a result, a smaller likelihood of the flare erupting. We conclude that a more detailed morphological study of J_z patterns in ARs hosting eruptive and confined events with analysis of preflare coronal images to track flux rope existence is needed to clarify the relationship between J_z morphology and the AR ability to erupt.

We also calculate the total and mean vertical current within the AR, ribbon, and PIL areas. We find that the total vertical current increases as we go from the PIL to AR areas, reflecting larger integration areas. On the other hand, the mean current decreases from the PIL to AR areas, since within the PIL and ribbon areas, magnetic fields are much more nonpotential than in the AR as a whole.

Net current within the AR, ribbons, and PILs. Understanding how currents are neutralized is important for numerical models of solar eruptions (see Introduction in Török et al. 2014). If we look at the AR as a whole, we find that $|DC/RC| \approx 1$; i.e., the current is neutralized, in agreement with previous studies (Wheatland 2000; Venkatakrishnan & Tiwari 2009; Georgoulis et al. 2012b). On the other hand, individual polarities contain a net current. This net current varies from 1 to 3 and is largest in the central part of the AR, around the PIL and ribbon areas, decreasing gradually within the polarity as a whole (an AR net current). In the simulations, net currents are larger but exhibit similar growth from the periphery to the center of the AR. For

example, using ARMS simulations, here we find net currents reaching up to 5 within individual AR polarities and 10 within the ribbon areas. For a simulation of an emerging AR, Török et al. (2014) found net currents reaching up to 5 and increasing as an AR emerges, consistent with preflare ARMS values. In their MHD simulations, Titov et al. (2008) and Aulanier et al. (2010) also found weak RCs with net currents around 3, similar to the observed values we find here with FlareMagDB.

What creates these net currents? Net currents could emerge bodily into the corona ("emergence"; e.g., Leka et al. 1996; Longcope & Welsch 2000) or be produced by stressing of the coronal magnetic field by subphotospheric and photospheric shearing flows ("shear"; e.g., McClymont & Fisher 1989; Török & Kliem 2003; Aulanier et al. 2010). From our statistical analysis, we find that the net current within each AR polarity (or ribbon) is proportional to magnetic shear at the PIL, with most of the DC lying in the PIL vicinity. In other words, the net current is a manifestation of the magnetic shear at the PIL. This conclusion is in agreement with recent findings using simulations (Török et al. 2014; Dalmasse et al. 2015) and one-case morphological studies using observations (Ravindra et al. 2011; Georgoulis et al. 2012a; Liu & Schuck 2012; Vemareddy 2015). Török et al. (2014) and Dalmasse et al. (2015) found that net currents are cotemporal with the surge of shear at the PIL and can be formed due to flux emergence, twisting and shearing motions, and any mechanism that can generate magnetic shear along a PIL. Using high-resolution vector magnetograms of an emerging AR over several days from the Spectropolarimeter/Hinode instrument, Ravindra et al. (2011) noticed that the net current within individual polarities could be related to shear at the PIL. In a different study, Venkatakrishnan & Tiwari (2009) found that nonsheared PILs have zero net current. In this paper, we perform a first quantitative analysis of a fairly large observation data set and find that the net current is proportional to the shear at the PIL. This finding is expected from the integral form of Ampère's law, $\oint \boldsymbol{B} \cdot dl = (4\pi/c)I$. While along the PIL, $\oint \boldsymbol{B} \cdot dl > 0$, along the curved segment away from the PIL, $\oint \boldsymbol{B} \cdot dl \approx 0$. The presence of the net current in our sample of ARs supports previous studies that state that RCs get trapped under the photosphere during flux emergence, leading to the presence of a net current causing increased shear at the PIL. Our results also confirm that coronal flux rope models that neglect RCs are a valid representation of preeruption configurations on the Sun.

Confined versus eruptive flares. Here we find that for a given X-ray flux, confined flares have smaller reconnection flux fractions, R_Φ (see triangles versus circles in Figure 6(b)). If we go one step further and look not just at the flare eruptivity but also at the CME speeds, we find that among all magnetic variables of FlareMagDB, the reconnection flux fraction is the only variable that has a strong correlation with the CME speed ($r_s = 0.6$; see Figure 5). Earlier, some indications of this relationship were suggested by Tschernitz et al. (2018), Toriumi et al. (2017) and Li et al. (2020). Tschernitz et al. (2018) analyzed 51 flares (32 confined, 19 eruptive) ranging from GOES class B3 to X17. They found that confined flares of a certain GOES class have smaller ribbon areas but larger mean magnetic fields. This result implies that confined flares occur closer to the flux-weighted center of ARs, where fields that could be swept by the flare ribbons could be stronger. In a different study, Toriumi et al. (2017) and Li et al. (2020) compared R_Φ in confined versus eruptive flares, finding that

eruptive events have, on average, larger flux fractions. Here, instead of a binary comparison between confined and eruptive event properties, we analyzed the CME speed for the first time. In Figure 8, we show the scatter plot of the CME speed versus the reconnection fraction with the functional fit of $y = ax + b$ describing the relationship, where $a = 32 \pm 9$ and $b = 290 \pm 180$, and $R^2 = 0.3$. If correct, the new relationship between the CME speed and the reconnection fraction could, in principle, be used to predict the CME speed once the solar flare occurs.

How could we explain the correlation between the CME speed and the reconnection flux fraction? We suggest the following scenario. Once the flare starts, reconnection starts feeding magnetic flux into a preexisting flux rope or a sheared arcade. As this new flux rope forms, overlying fields within an AR provide a retrieving force to keep this flux rope stable. As a result, the larger the reconnection flux fraction, the weaker the restraining arcade above and the faster the new flux rope erupts, reaching torus instability at a lower height (Chen et al. 2019; Kliem et al. 2021). The torus instability occurs when the overlying potential arcade decays with a critical index, $n_{\mathrm{crit}} = -\frac{d \ln B}{d \ln z} \approx 1.1\text{–}1.5$, depending on the flux rope geometry and shear in the overlaying arcade (Kliem & Török 2006). If the tension of the arcade above is not sufficient, the flux rope starts expanding, thinning the reconnection current sheet further and causing more reconnection to take place. This scenario accounts for the slow rise of filaments based on tether-cutting-like reconnection (Moore et al. 2001) and the fast eruption after the torus instability kicks in. It is also in line with a recent observation analysis by Li et al. (2020, 2021), who analyzed 322 and 719 flares, respectively, and found that the flare–CME association rate decreases with the increasing magnetic flux of the AR that produces the flare, implying that a large magnetic flux tends to confine eruptions.

Physically, the reconnection flux fraction represents the ratio between the flux gained by the nonpotential flux rope and the total more potential flux of the AR. Lin et al. (2021) generalized this idea, calling it the "relative nonpotentiality" of a magnetic flux rope. Consistent with the scenario above, a larger relative nonpotentiality indicates a higher probability for a flux rope to erupt. Section 1 of Lin et al. (2021) contains a nice overview of a variety of schemes to quantitatively evaluate the relative nonpotentiality.

We find that all of the confined events in our data set have a reconnection flux fraction, $R_\Phi < 15\%$, below the instability criteria, $R_{\Phi,\mathrm{inst}} \approx 30\%$, determined by the use of the flux rope insertion method (Savcheva & van Ballegooijen 2009; Su et al. 2011; Savcheva et al. 2012b). (For comparison, the typical 20th–80th percentile for the reconnection flux fraction in `FlareMagDB` is $R_\Phi[P_{20}, P_{80}] = [8.2, 20.1]\%$, and the ARMS value is $R_\Phi \approx 43\%$.) On the other hand, as seen from the CME speed versus reconnection flux fraction plot in Figure 8, there are many events that are eruptive and yet have a reconnection flux fraction below the instability criterion, $R_{\Phi,\mathrm{inst}} \approx 30\%$. A systematic analysis of these outlier events would be interesting to understand why these events are eruptive.

Compared to eruptive events, we find that confined events tend to have stronger PIL fluxes. We speculate that for a constant amount of flux in the flux rope, a stronger vertical PIL flux implies a weaker horizontal flux and, as a result, smaller magnetic energy within a flux rope.

We also compare PIL shear (and a related ribbon net current) for confined versus eruptive events and find that confined events have a smaller PIL shear and ribbon net current. This result statistically confirms the earlier studies of Liu et al. (2017; four events), Avallone & Sun (2020; 30 events), and Kontogiannis et al. (2019; 32 events), who found that flare-/CME-active ARs are associated with larger net currents than flare-/CME-quiet ARs. For our limited data set, however, this relationship is not very strong, with a large number of outliers; i.e., there are many eruptive events with a small net current, as was previously noted by Avallone & Sun (2020). Case studies of these events might be useful to understand the relationship between eruptivity and the net current. From a physics standpoint, we explain the lack of shear in confined events by a smaller nonpotential energy and hence a smaller likelihood to erupt.

We note that all of our conclusions regarding confined versus eruptive events are limited by the small number of confined events we analyzed (seven events). Extension of this work to a larger sample of confined and eruptive events would be necessary to draw more confident conclusions.

6. Conclusions

In this paper, we analyzed the preflare vector magnetic fields within AR, flare ribbon, and PIL areas in 40 events and ARMS eruption simulations with the objective of improving our understanding of the physical properties of flaring versus nonflaring photospheric vector magnetic fields in the photosphere.

Our quantitative findings are as follows.

1. *Ribbon versus PIL morphology.* Qualitatively, comparing the near-PIL areas and flare ribbons in observations and simulations (Figures 2 and 10), we find that the morphology of PILs has almost no bearing on the morphology of flare ribbons. Hence, while one can accept Schrijver's (2007) contention that larger amounts of near-PIL flux indicate a greater likelihood of a larger flare, the spatial arrangement of the PIL does not substantively constrain the ribbons' spatial distribution.

2. *Magnetic fluxes.* We find strong statistical correlations between the flare peak X-ray flux and the flare ribbon and PIL fluxes (Figure 6(a)): Spearman correlation coefficient $r_s(I_{\mathrm{X,peak}}, \Phi_{\mathrm{ribbon}}) = 0.9$ and $r_s(I_{\mathrm{X,peak}}, \Phi_{\mathrm{PIL}}) = 0.6$, respectively, in agreement with Kazachenko et al.'s (2017) analysis. While the correlation between flare size and PIL flux is in line with Schrijver's (2007) hypothesis that flare-productive ARs tend to have stronger PILs, it could reflect the fact that larger ARs have stronger PILs and hence host larger flares. The correlation between the peak X-ray flux and the corresponding AR quantities is weaker, ranging from $r_s(I_{\mathrm{X,peak}}, \Phi_{\mathrm{AR}}) = 0.3$ for the full data set ($n = 3137$, `RibbonDB`; Kazachenko et al. 2017) to $r_s(I_{\mathrm{X,peak}}, \Phi_{\mathrm{AR}}) = 0.6$ for `FlareMagDB` ($n = 40$).

3. *Reconnection flux fractions.* We find a moderate correlation between the flare peak X-ray flux and the fraction of AR magnetic flux participating in the flare, consistent with earlier results (Figure 6(b)).

4. *Mean magnetic shears.* In both observations and simulations, we find that the mean magnetic shear is strongest within the PIL areas, decreasing gradually within ribbon and AR areas (Figure 6(c)): $\alpha(\mathrm{AR}, \mathrm{rbn}, \mathrm{PIL}) =$

$[10, 18, 26] \times 10^3 \, \text{G}^\circ$ for `RibbonDB` versus α(AR, rbn, PIL) $= [0.06, 0.13, 0.17] \times 10^3 \, \text{G}^\circ$ for ARMS. The peak X-ray flux is moderately correlated with the mean magnetic shear within the AR and weakly correlated with the mean magnetic shear within the ribbon and PIL areas.

5. *Current density morphology.* Qualitatively, current density maps consist of threadlike and patchy structures that do not exhibit any regular shape or correlate with ribbon locations, flares, and/or CME occurrence (Figure 12).

6. *Total vertical currents.* We find that the total area-integrated unsigned vertical current is largest within the AR areas, decreasing gradually within the ribbon and PIL areas (Figure 6(d)).

7. *Net currents.* Over the entire AR, we find that the currents are neutralized, in agreement with earlier studies (orange symbols in Figure 7(a)):

$$(DC/RC)_{AR} = 0. \qquad (18)$$

Over one polarity (positive or negative), the currents are nonneutralized (blue symbols in Figure 7(a)):

$$(DC/RC)_{AR,+} \approx -(DC/RC)_{AR,-} \neq 0. \qquad (19)$$

The central part of the AR around the PIL has the highest net current, decreasing gradually within the ribbon and AR areas (see red, green, and blue symbols, Figure 7(a)). We find that the net current within the flare ribbons strongly correlates with the mean magnetic shear within the PIL (Figure 7(b), $r_s = 0.7$) with the scaling relationship $|DC/RC| \propto 0.02 \bar{\alpha}_{PIL} + 0.9$, implying that current nonneutralization is a manifestation of the shear accumulation along the PIL, in agreement with simulations (Török et al. 2014; Dalmasse et al. 2015).

8. *Confined versus eruptive flares.* We find that for a given peak X-ray flux, confined events have larger PIL fluxes and lower mean PIL shears and ribbon net currents than eruptive events (see triangles versus circles in Figures 6(a), (c), and (d)), in agreement with Liu et al. (2017) and Avallone & Sun (2020). We also find that the CME speed has a strong correlation with the fraction of the AR that participates in the flare (Figure 8). In fact, the flux ratio is the only variable that has a correlation coefficient with a CME speed above $r_s > 0.4$.

To summarize, following Welsch et al.'s (2009) "intensive–extensive" classification, our analysis suggests that while flare peak X-ray fluxes are guided by extensive magnetic field properties that scale with the AR size (like the total amount of magnetic flux that participates in the reconnection process; Bobra & Couvidat 2015), the CME speeds are guided by intensive properties that do not scale with the AR size (like the fraction between the reconnection flux and the AR flux, defined by the amount of overlying field; Sun et al. 2015; Bobra & Ilonidis 2016), with little dependence on the amount of mean PIL shear or net current.

This study is the largest statistical analysis yet of the flare vector magnetic fields within flare ribbon and PIL areas and the relationship with other flare and AR properties. Such a statistical approach is useful, since it allows us to discover general laws that may be overlooked by individual case studies.

The `FlareMagDB` catalog is available online[9] in CSV and IDL sav file formats, along with maps of vector magnetic fields, magnetic shear, current densities, the PIL, and ribbon masks, and can be used for different types of quantitative studies in the future, from constraining the properties of the simulations to further detailed observation studies. For example, a comparison of magnetic field properties with the presence of sigmoidal structures or filaments would be valuable to clarify the relationship between the coronal structures and the photospheric magnetic fields. Analysis of the outliers in the derived trends—for example, events with a large magnetic shear and small net current, and vice versa—would be interesting. Extension of this statistical work to a larger number of confined flares observed over a decade of SDO, including temporal evolution of the magnetic field properties over the flare (e.g., Barczynski et al. 2020; Sharykin et al. 2020), would allow us to further advance our understanding of solar eruption magnetism.

Appendix
`FlareMagDB` for All Events: Magnetic Shear and Vertical Current Maps

Figures 11 and 12 show magnetic field shear and vertical current distributions maps for 40 events in the `FlareMagDB` database, respectively.
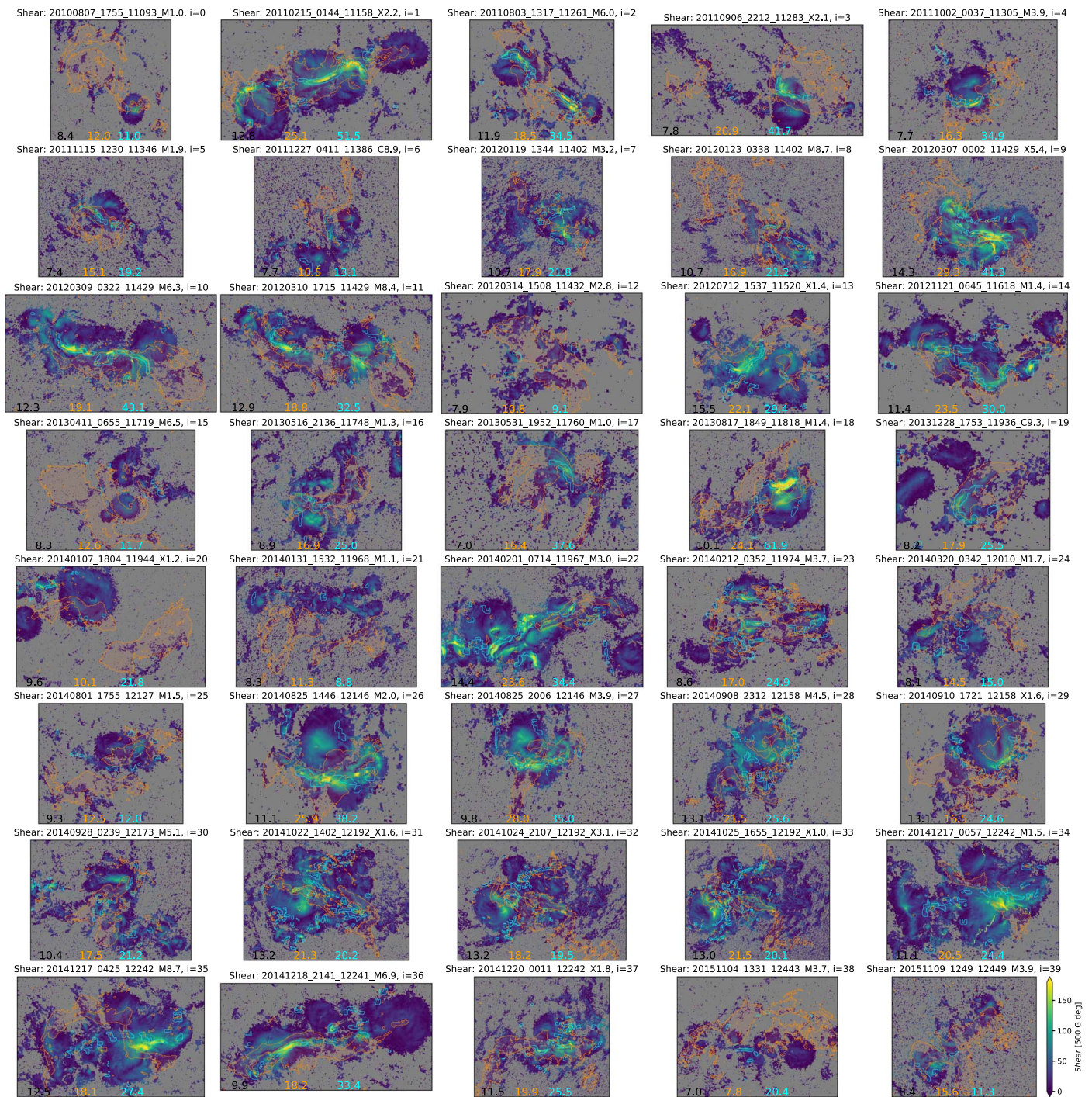
---

9   http://solarmuri.ssl.berkeley.edu/~kazachenko/FlareMagDB/

Figure 11. Magnetic field shear, α, for 40 events from the `FlareMagDB` database. Black, orange, and cyan numbers indicate the mean magnetic shear within the AR, ribbon, and PIL areas, respectively (see column $\bar{\alpha}$ in Table 1).
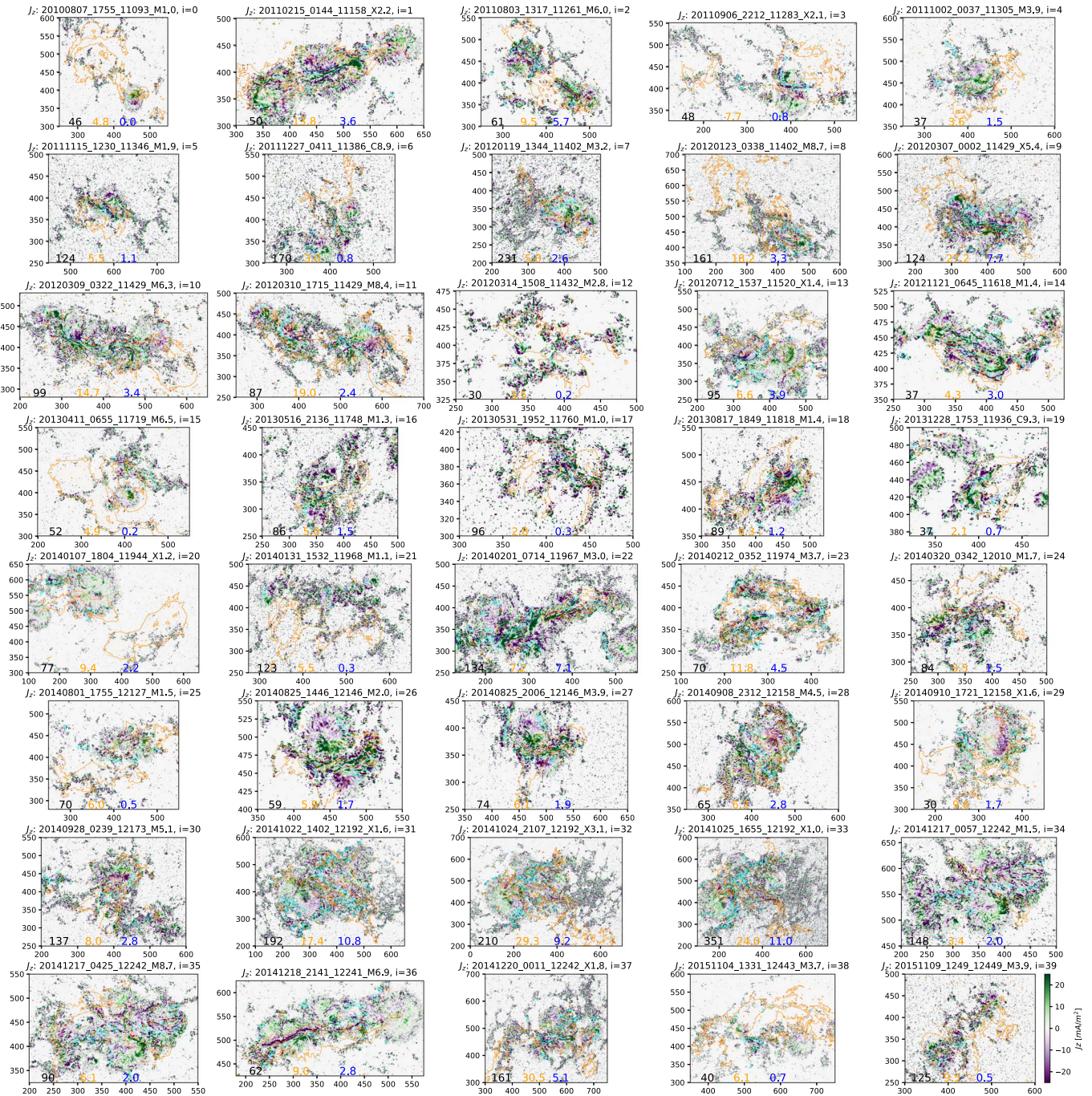
Figure 12. Vertical current distribution, J_z, for 40 events from the FlareMagDB database. Black, orange, and blue numbers indicate the total electric current within the AR, ribbon, and PIL areas, respectively (see column $I_{z,u}$ in Table 1).

ORCID iDs

Maria D. Kazachenko ● https://orcid.org/0000-0001-8975-7605
Benjamin J. Lynch ● https://orcid.org/0000-0001-6886-855X
Antonia Savcheva ● https://orcid.org/0000-0002-5598-046X
Xudong Sun ● https://orcid.org/0000-0003-4043-616X
Brian T. Welsch ● https://orcid.org/0000-0003-2244-641X

References

Antiochos, S. K., DeVore, C. R., & Klimchuk, J. A. 1999, ApJ, 510, 485
Aulanier, G., Janvier, M., & Schmieder, B. 2012, A&A, 543, A110
Aulanier, G., Török, T., Démoulin, P., & DeLuca, E. E. 2010, ApJ, 708, 314
Avallone, E. A., & Sun, X. 2020, ApJ, 893, 123

Barczynski, K., Aulanier, G., Janvier, M., Schmieder, B., & Masson, S. 2020, ApJ, 895, 18
Bobra, M. G., & Couvidat, S. 2015, ApJ, 798, 135
Bobra, M. G., & Ilonidis, S. 2016, ApJ, 821, 127
Canfield, R. C., Kazachenko, M. D., Acton, L. W., et al. 2007, ApJL, 671, L81
Carmichael, H. 1964, NASSP, 50, 451
Chen, J., Kliem, B., & Liu, R. 2019, in 21st EGU General Assembly (EGU2019), 10039, https://www.egu2019.eu/
Chintzoglou, G., Zhang, J., Cheung, M. C. M., & Kazachenko, M. 2019, ApJ, 871, 67
Dahlin, J. T., Antiochos, S. K., & DeVore, C. R. 2019, ApJ, 879, 96
Dalmasse, K., Aulanier, G., Démoulin, P., et al. 2015, ApJ, 810, 17
DeVore, C. R., & Antiochos, S. K. 2008, ApJ, 680, 740
Fisher, G. H., Welsch, B. T., Abbett, W. P., & Bercik, D. J. 2010, ApJ, 715, 242

Georgoulis, M. K., Nindos, A., & Zhang, H. 2019, RSPTA, 377, 20180094
Georgoulis, M. K., Titov, V. S., & Mikić, Z. 2012a, ApJ, 761, 61
Georgoulis, M. K., Tziotziou, K., & Raouafi, N.-E. 2012b, ApJ, 759, 1
Gosain, S., & Venkatakrishnan, P. 2010, ApJL, 720, L137
Hirayama, T. 1974, SoPh, 34, 323
Hoeksema, J. T., Liu, Y., Hayashi, K., et al. 2014, SoPh, 289, 3483
Janvier, M. 2016, JPlPh, 83, 535830101
Janvier, M., Démoulin, P., & Dasso, S. 2014, SoPh, 289, 2633
Karna, N., Savcheva, A., Gibson, S., et al. 2021, ApJ, 913, 47
Karpen, J. T., Antiochos, S. K., & DeVore, C. R. 2012, ApJ, 760, 81
Kazachenko, M. D., Canfield, R. C., Longcope, D. W., & Qiu, J. 2010, ApJ, 722, 1539
Kazachenko, M. D., Canfield, R. C., Longcope, D. W., & Qiu, J. 2012, SoPh, 277, 165
Kazachenko, M. D., Lynch, B. J., Welsch, B. T., & Sun, X. 2017, ApJ, 845, 49
Kliem, B., Su, Y. N., van Ballegooijen, A. A., & DeLuca, E. E. 2013, ApJ, 779, 129
Kliem, B., & Török, T. 2006, PhRvL, 96, 255002
Kliem, B., Zhang, J., Torok, T., & Chintzoglou, G. 2021, in 43rd COSPAR Scientific Assembly, 997, https://cospar2021.org/
Kontogiannis, I., Georgoulis, M. K., Guerra, J. A., Park, S.-H., & Bloomfield, D. S. 2019, SoPh, 294, 130
Kopp, R. A., & Pneuman, G. W. 1976, SoPh, 50, 85
Leka, K. D., Canfield, R. C., McClymont, A. N., & van Driel-Gesztelyi, L. 1996, ApJ, 462, 547
Lemen, J. R., Title, A. M., Akin, D. J., et al. 2012, SoPh, 275, 17
Li, T., Chen, A., Hou, Y., et al. 2021, ApJL, 917, L29
Li, T., Hou, Y., Yang, S., et al. 2020, ApJ, 900, 128
Lin, P. H., Kusano, K., & Leka, K. D. 2021, ApJ, 913, 124
Liu, Y., & Schuck, P. W. 2012, ApJ, 761, 105
Liu, Y., Sun, X., Török, T., Titov, V. S., & Leake, J. E. 2017, ApJL, 846, L6
Longcope, D., Beveridge, C., Qiu, J., et al. 2007, SoPh, 244, 45
Longcope, D. W., & Welsch, B. T. 2000, ApJ, 545, 1089
Lynch, B. J., Airapetian, V. S., DeVore, C. R., et al. 2019, ApJ, 880, 97
Lynch, B. J., Antiochos, S. K., DeVore, C. R., Luhmann, J. G., & Zurbuchen, T. H. 2008, ApJ, 683, 1192
Lynch, B. J., Antiochos, S. K., Li, Y., Luhmann, J. G., & DeVore, C. R. 2009, ApJ, 697, 1918
Lynch, B. J., & Edmondson, J. K. 2013, ApJ, 764, 87
Lynch, B. J., Palmerio, E., DeVore, C. R., et al. 2021, ApJ, 914, 39
McClymont, A. N., & Fisher, G. H. 1989, in Yosemite Conference on Outstanding Problems in Solar System Plasma Physics: Theory and Instrumentation, ed. J. H. Waite, J. L. Burch, & R. L. Moore, Vol. 54 (Washington, DC: American Geophysical Union), 219
Moore, R. L., Sterling, A. C., Hudson, H. S., & Lemen, J. R. 2001, ApJ, 552, 833

Pesnell, W. D., Thompson, B. J., & Chamberlin, P. C. 2012, SoPh, 275, 3
Petrie, G. J. D. 2019, ApJS, 240, 11
Ravindra, B., Venkatakrishnan, P., Tiwari, S. K., & Bhattacharyya, R. 2011, ApJ, 740, 19
Savcheva, A., Pariat, E., McKillop, S., et al. 2015, ApJ, 810, 96
Savcheva, A., Pariat, E., McKillop, S., et al. 2016, ApJ, 817, 43
Savcheva, A., Pariat, E., van Ballegooijen, A., Aulanier, G., & DeLuca, E. 2012a, ApJ, 750, 15
Savcheva, A., & van Ballegooijen, A. 2009, ApJ, 703, 1766
Savcheva, A. S., Green, L. M., van Ballegooijen, A. A., & DeLuca, E. E. 2012b, ApJ, 759, 105
Savcheva, A. S., McKillop, S. C., McCauley, P. I., Hanson, E. M., & DeLuca, E. E. 2014, SoPh, 289, 3297
Savcheva, A. S., van Ballegooijen, A. A., & DeLuca, E. E. 2012c, ApJ, 744, 78
Scherrer, P. H., Schou, J., Bush, R. I., et al. 2012, SoPh, 275, 207
Schmieder, B., & Aulanier, G. 2018, in Electric Currents in Geospace and Beyond, ed. A. Keiling, O. Marghitu, & M. Wheatland (Washington, DC: American Geophysical Union), 391
Schrijver, C. J. 2007, ApJL, 655, L117
Sharykin, I. N., Zimovets, I. V., & Myshyakov, I. I. 2020, ApJ, 893, 159
Sturrock, P. A. 1968, in IAU Symp. 35, Structure and Development of Solar Active Regions, ed. K. O. Kiepenheuer (Dordrecht: D. Reidel), 471
Su, Y., Surges, V., van Ballegooijen, A., DeLuca, E., & Golub, L. 2011, ApJ, 734, 53
Sun, X., Bobra, M. G., Hoeksema, J. T., et al. 2015, ApJL, 804, L28
Sun, X., & Cheung, M. C. M. 2021, SoPh, 296, 7
Sun, X., Hoeksema, J. T., Liu, Y., Kazachenko, M., & Chen, R. 2017, ApJ, 839, 67
Titov, V. S., Mikic, Z., Linker, J. A., & Lionello, R. 2008, ApJ, 675, 1614
Toriumi, S., Schrijver, C. J., Harra, L. K., Hudson, H., & Nagashima, K. 2017, ApJ, 834, 56
Toriumi, S., & Wang, H. 2019, LRSP, 16, 3
Török, T., & Kliem, B. 2003, A&A, 406, 1043
Török, T., Leake, J. E., Titov, V. S., et al. 2014, ApJL, 782, L10
Tschernitz, J., Veronig, A. M., Thalmann, J. K., Hinterreiter, J., & Pötzi, W. 2018, ApJ, 853, 41
Vemareddy, P. 2015, ApJ, 806, 245
Venkatakrishnan, P., & Tiwari, S. K. 2009, ApJL, 706, L114
Wang, H., Liu, C., Ahn, K., et al. 2017, NatAs, 1, 0085
Warren, H. P., & Antiochos, S. K. 2004, ApJL, 611, L49
Welsch, B. T., Li, Y., Schuck, P. W., & Fisher, G. H. 2009, ApJ, 705, 821
Wheatland, M. S. 2000, ApJ, 532, 1209
Wyper, P. F., Antiochos, S. K., DeVore, C. R., et al. 2021, ApJ, 909, 54
Yashiro, S., Akiyama, S., Gopalswamy, N., & Howard, R. A. 2006, ApJL, 650, L143